JM PAPERS

Deformation, dynamics and rheology of immersed elastic capsules in an inertial shear flow

Guodong Gai[1] , **Damien P. Huet**,[1] **Jiahao Gong**[1] **and Anthony Wachs**[1,2]

[1]Department of Mathematics, University of British Columbia, Vancouver, BC, Canada

[2]Department of Chemical & Biological Engineering, University of British Columbia, Vancouver, BC, Canada

Corresponding author: Anthony Wachs, wachs@math.ubc.ca

We investigate the deformation, dynamics and rheology of a single and a suspension of elastic capsules in inertial shear flow using high-fidelity particle-resolved simulations. For a single capsule in the shear flow, we elucidate the interplay of flow inertia and viscosity ratio, revealing the mechanism behind the stretching of capsule surface during tank-treading motion and the sign changes in normal stress differences with increasing inertia. When examining capsule suspensions, we thoroughly discuss the impact of volume fraction on average deformation, diffusion and rheology. Notably, we observe the formation of bridge structures due to hydrodynamic interactions, which enhance the inhomogeneity of the microstructure and alter the surface stress distribution within the suspension. We identify a critical Reynolds number range that marks the transition of capsule diffusion from non-inertial to inertial regimes. Furthermore, we reveal close connections between the behaviour of individual capsules and dense suspensions, particularly regarding capsule deformation and dynamics. Additionally, we propose multiple new empirical correlations for predicting the deformation factor of a single capsule and the relative viscosity of the suspension. These findings provide valuable insights into the complex behaviour of elastic capsules in inertial flows, informing the design of more accurate and efficient inertial microfluidic systems.

Key words: suspensions, capsule/cell dynamics

1. Introduction

Capsules, membrane-enclosing fluid objects, play pivotal roles across many natural and industrial domains, including the biological, pharmaceutical, cosmetic and food

industries (Barthes-Biesel 2016; Luo & Bai 2019; Sun *et al.* 2021). Capsules also serve as simplified models for examining complex biological cells, such as red blood cells (RBCs) and circulating tumour cells, through numerical analysis (Krüger 2012; Gekle 2016; Balogh *et al.* 2021; Huet & Wachs 2023). Given their significant role and applications, understanding and manipulating capsules require advanced theoretical, experimental and numerical techniques. Recent advances have highlighted the utility of microfluidic devices in separating cells by size and deformability, enriching specific cell concentrations, and facilitating precise cell characterisation (Häner *et al.* 2021; Wang *et al.* 2016). Enhanced computing capabilities have further bolstered the design and optimisation of these devices, enabling sophisticated numerical analyses that mimic experimental conditions (Zhu *et al.* 2014; Gubspun *et al.* 2016). Notably, innovative microfluidic designs, such as a semi-circular pillar geometry developed and optimised numerically by Zhu *et al.* (2014), have demonstrated efficacy in sorting cells based on membrane stiffness, confirmed through both numerical studies and experimental validations (Häner *et al.* 2021).

Over the last years, considerable research efforts have been directed towards modelling and understanding the deformation and dynamics of capsules in non-inertial flows, a focus driven largely by its relevance to microcirculatory systems such as capillary blood vessels and conventional microfluidic applications. Based on the thin-shell theory, Barthès-Biesel and Rallison initially provided an analytical framework for the temporal evolution of elastic capsule deformation under infinite, slow-moving shear flows, assuming infinitesimal deformations (Barthes-Biesel & Rallison 1981). Subsequently, Pozrikidis expanded on this by applying the boundary integral method to accommodate finite deformations (Pozrikidis 1995), a method further applied to analyse significant deformation in capsules with distinct internal and external fluid viscosities (Ramanujan & Pozrikidis 1998), and to incorporate the effects of bending stresses (Pozrikidis 2001). In terms of the capsule dynamics, it was shown that the migration and diffusion of a capsule suspension do differ from those of hard sphere suspensions due to the deformable capsule–capsule interactions and the dissipating inner fluid (Bishop *et al.* 2002; Kulkarni & Morris 2008; Gross *et al.* 2015; Rahmani *et al.* 2018). More recently, Balogh and Bagchi (Balogh & Bagchi 2017, 2018, 2019) employed the front-tracking method (FTM) to delve into the behaviour and structural changes of RBCs within the complex vessel networks reminiscent of human microcirculation. Apart from the migration of capsules in channels of different geometries, the mechanical and rheological properties of suspensions of purely elastic capsules have been thoroughly studied in the non-inertial regime. The rheological behaviour of suspensions, especially for the rigid particles, was addressed in the pioneering work of Batchelor (1970), establishing that stresses due to the presence of particles are formulated using a particle stress tensor, which can be expressed as a summation of stresslets in a domain. Recently, Takeishi *et al.* (2019) conducted a comprehensive investigation of the rheology of a suspension of RBCs in a wall-bounded shear flow, highlighting that the dynamic motion of RBCs has an important influence on the suspension rheology. Aouane *et al.* (2021) reveal that the strain-hardening capsules share rheological features with both soft and solid particles depending on the ratio of the area dilatation to shear elastic modulus and the effective volume fraction. Guglietta *et al.* (2023) studied the suspension of viscoelastic capsules by considering the effects of membrane viscosity on the transient dynamics of the suspension rheology. They showed that the influence of the membrane viscosity strongly depends on the capsule volume fraction.

Inertial particle microfluidics has recently emerged as a cutting-edge technique for high-precision and efficient manipulation of microparticles and biological cells. This technology finds application in fields ranging from microbiology to biotechnology, offering a promising avenue to expedite labour-intensive, non-destructive diagnostic processes such as cell sorting and cell characterisation (Krüger *et al.* 2014; Son *et al.* 2017; Yin *et al.* 2019; Owen *et al.* 2023). Given the substantially higher flow velocities in inertial microfluidics compared with their non-inertial counterparts, traditional analytical theories and methods relying on the Stokes conditions such as the boundary integral method fail to account for the advective components of the fluid momentum equation (Amini *et al.* 2014). Initial investigations into the inertial dynamics of capsules, such as the work of Doddi & Bagchi (2008), who explored the interactions and spiralling motions of two capsules in a shear flow using the FTM, laid the groundwork for this field. Research into the dynamics of deformable capsules in inertial flows has revealed distinct behaviours depending on channel geometry. Subsequent studies in straight microchannels identified multiple equilibrium positions for deformable capsules, diverging from the channel centreline towards the cross-section diagonals, and primarily influenced by inertial forces: wall repulsion, shear-gradient lift and drag forces in secondary flow fields (Kilimnik *et al.* 2011; Raffiee *et al.* 2017; Owen *et al.* 2023). Building on this, Ebrahimi & Bagchi (2021) extended the analysis to curved channels, systematically varying parameters such as channel Reynolds number, capsule deformability and channel geometry to uncover the effects of curvature on the capsule dynamics. Parallel advancements have focused on other deformable particles, notably droplets, whose behaviours under finite inertia have been extensively explored. These studies highlight insights into the dynamics of emulsions, emphasising the effects of inclination angles on rheological behaviours (Li & Sarkar 2005*b*; Olapade *et al.* 2009; Singh & Sarkar 2009; Singh & Sarkar 2011, 2015). For elastic capsule suspensions specifically, Banaei *et al.* examined nucleated capsules under finite inertia (Banaei *et al.* 2017, 2021), showing significant effects on deformation and suspension rheology, including increased relative viscosity. In our previous work (Huet *et al.* 2024), we further investigated the dynamics of elastic capsule trains navigating sharp corners under inertial flow, identifying mechanisms behind interaction and deformation in these complex geometries.

Despite the existing body of knowledge previously summarised, significant gaps still remain in our understanding of the deformation, diffusion and rheology of elastic capsule suspensions in an inertial shear flow. Current research has yet to comprehensively address the intricate interactions and behaviours that arise under varying conditions of inertia and flow dynamics. We aim to answer the following questions using high-fidelity particle-resolved numerical simulations: (i) How does flow inertia impact the deformation and dynamics of a single capsule in a shear flow? (ii) What are the connections between the behaviour of a single capsule and that of a dense suspension? (iii) What are the major differences between capsule suspensions in the non-inertial and inertial regimes?

This manuscript is organised as follows: § 2 provides the governing equations and membrane models for the deformable capsule. In § 3, we introduce the numerical set-ups for a single capsule and a capsule suspension in a shear flow. The novel findings for a single capsule in a shear flow are presented in § 4. In § 5, we present the numerical results on the deformation, lateral migration and rheology of the capsule suspension and discuss their relationship with the behaviour observed in single capsule studies. Finally, § 6 provides the conclusions and perspectives for future investigation.

2. Numerical method and dimensionless numbers

2.1. *Governing equation and membrane models*

The capsule membrane $\tilde{\Gamma}$ is assumed infinitely thin and is surrounded by an incompressible Newtonian fluid with constant viscosity and density. In this study, the viscosity ratio between the inner and outer fluids of the capsule may differ from unity. The fluid dynamics is governed by the mass and momentum conservation equations

$$\tilde{\nabla} \cdot \tilde{\boldsymbol{u}} = 0, \tag{2.1}$$

$$\frac{\partial \tilde{\boldsymbol{u}}}{\partial \tilde{t}} + \tilde{\boldsymbol{u}} \cdot \tilde{\nabla} \tilde{\boldsymbol{u}} = \frac{1}{\tilde{\rho}} \tilde{\nabla} \tilde{p} + \tilde{\nu} \tilde{\nabla}^2 \tilde{\boldsymbol{u}} + \frac{1}{\tilde{\rho}} \tilde{\boldsymbol{f_b}}, \tag{2.2}$$

where $\tilde{\boldsymbol{u}}$ denotes the velocity field, $\tilde{p}$ the pressure field and $\tilde{\rho}$ the density. The kinematic viscosity is given by $\tilde{\nu} = \tilde{\mu}/\tilde{\rho}$, where $\tilde{\mu}$ is the dynamic viscosity. The term $\tilde{\boldsymbol{f_b}}$ represents a body force that accounts for the influence of the capsule membrane on its surrounding fluid. Dimensional quantities are indicated by the $\sim$ symbol. The membrane can exhibit both elasticity and bending stresses, and its localised action on the fluid is described by the following expression for $\tilde{\boldsymbol{f_b}}$:

$$\tilde{\boldsymbol{f_b}} = \left(\tilde{\boldsymbol{F}}_{elastic} + \tilde{\boldsymbol{F}}_{bending} \right) \tilde{\delta}(\tilde{\boldsymbol{x}} - \tilde{\boldsymbol{x_0}}), \tag{2.3}$$

where $\tilde{\boldsymbol{x}} = (\tilde{x}, \tilde{y}, \tilde{z})$ is the position vector and $\tilde{\delta}(\tilde{\boldsymbol{x}} - \tilde{\boldsymbol{x_0}})$ is a Dirac delta distribution defined at position $\tilde{\boldsymbol{x_0}}$, which is non-zero only on the surface of the membrane since $\tilde{\boldsymbol{x_0}} \in \tilde{\Gamma}$. Please note that only the elastic force is considered in the current research, while bending stresses are neglected.

The shear and area-dilatation membrane stresses are described using the thin-shell theory, which is briefly summarised here. For more detailed information, readers are referred to the analytical study by Barthes-Biesel & Rallison (1981). In this work, we adopt the Skalak law to describe the elastic membrane, with the expression of the surface strain energy function $\tilde{W}_s$ expressed as

$$\tilde{W}_s = \frac{\tilde{E}_s}{4} \left(I_1^2 + 2I_1 - 2I_2 + C I_2^2 \right). \tag{2.4}$$

The two invariants are defined as $I_1 = \lambda_1^2 + \lambda_2^2 - 2$ and $I_2 = \lambda_1^2 \lambda_2^2 - 1$, where $\lambda_{1,2}$ are the principal stretches in the two tangential directions, and $\tilde{E}_s$ is the shear modulus. The constant $C = 1$ represents the area-dilatation modulus, which prevents significant area changes (Pozrikidis 1995). Subsequently, the membrane elastic stresses $\tilde{\sigma}_{i,j}$ are calculated using the surface strain energy function $\tilde{W}_s$

$$\tilde{\sigma}_{i,j} = \frac{1}{\lambda_j} \frac{\partial \tilde{W}_s}{\partial \lambda_i}, \qquad i, j \in \{1, 2\}, \quad i \neq j. \tag{2.5}$$

Once the elastic stress is determined, the elastic force exerted by the membrane on the fluid is calculated as follows:

$$\tilde{\boldsymbol{F}}_{elastic} = \tilde{\nabla} \cdot \tilde{\boldsymbol{\sigma}}. \tag{2.6}$$

The adaptive FTM is employed to solve the aforementioned equations. A concise overview of the numerical approach is provided in Appendix A. Equations (2.1) and (2.2) are spatially discretised using the finite volume method on an adaptive octree grid, or on a homogeneous Cartesian grid for capsule suspensions; and are implemented within

Parameter	Expression	Range	Symbol descriptions
Reynolds number	$\mathcal{R}e = \dfrac{\tilde{\rho}\tilde{\dot{\gamma}}\tilde{r}_0^2}{\tilde{\mu}_0}$	[0.1, 20]	$\tilde{\rho}$ fluid density
			$\tilde{r}_0$ radius of spherical capsule
			$\tilde{\dot{\gamma}}$ shear rate
			$\tilde{\mu}_0$ fluid dynamic viscosity
Capillary number	$\mathcal{C}a = \dfrac{\tilde{\mu}_0\tilde{\dot{\gamma}}\tilde{r}_0}{\tilde{E}_s}$	[0.01, 1]	$\tilde{E}_s$ membrane elastic modulus
volume fraction	$\phi = \dfrac{4N\pi\tilde{r}_0^3}{3\tilde{V}}$	[0.0008, 0.4]	$\tilde{V}$ computational domain volume
			N number of capsules in $\tilde{V}$
Viscosity ratio	$\lambda = \dfrac{\tilde{\mu}_{int}}{\tilde{\mu}_0}$	[1, 5]	$\tilde{\mu}_{int}$ capsule interior viscosity

Table 1. Flow control parameters for numerical simulations: mathematical expressions, range of values and detailed symbol descriptions.

the open-source software Basilisk (Popinet 2015). A comprehensive description of the numerical implementation is available in Huet & Wachs (2023).

2.2. *Physical quantities and dimensionless numbers*

Our problem is governed by several dimensionless numbers that describe and control the flow configuration. These include the Reynolds number $\mathcal{R}e$, which measures the ratio of inertial to viscous forces; the capillary number $\mathcal{C}a$, representing the ratio of viscous to elastic stresses; the capsule volume fraction ϕ, indicating the ratio of volume occupied by the capsules; and the fluid viscosity ratio λ of the internal and external fluids of the capsules. Please note that we adopt $\tilde{r}_0$ and $\tilde{\dot{\gamma}}\tilde{r}_0$ as length scale and velocity scale, respectively. For brevity, we summarise the key input parameters of the flow configuration in table 1, which presents the mathematical expression and range of values of each parameter, together with associated symbols and the corresponding descriptions.

As for the output parameters, we investigate various physical quantities of capsules in an inertial shear flow, including the Taylor deformation factor (D), particle stress (Σ), relative viscosity (μ_r) and capsule diffusivity (D_ψ). Below, we briefly outline the methods used to compute and normalise these physical quantities.

The information on the deformation of the capsules is retrieved from the moment of inertia tensor. We consider the ellipsoid with the same inertia tensor $\tilde{\mathcal{I}}$ as the capsule. Once we obtain the three eigenvalues ($\tilde{\zeta}_1 < \tilde{\zeta}_2 < \tilde{\zeta}_3$) of $\tilde{\mathcal{I}}$, we can use them to compute the length of the three semi-axes : $\tilde{r}_1$, $\tilde{r}_2$ and $\tilde{r}_3$ (Ramanujan & Pozrikidis 1998; Guglietta *et al.* 2023). Here, $\tilde{r}_1$ and $\tilde{r}_3$ are the longest and shortest lengths of the semi-axis in the shear plane ($x-y$ plane), and $\tilde{r}_2$ denotes the radius along the vorticity direction along the axis normal to the shear plane (z-axis). Subsequently, the Taylor deformation factor is defined as

$$D = \frac{\tilde{r}_1 - \tilde{r}_3}{\tilde{r}_1 + \tilde{r}_3}. \tag{2.7}$$

Figure 1 presents a brief sketch illustrating the two main semi-axes r_1, r_3 and the inclination angle θ of the capsule in shear flow on a $x-y$ cut plane crossing the
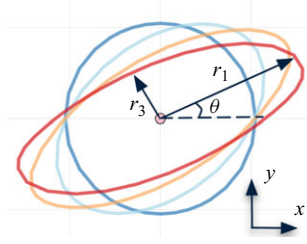
Figure 1. Sequential illustration of a spherical capsule's deformation in the shear plane. Transitioning from blue to red depicts the deformation dynamics of a spherical capsule. Here, r_1, r_3 and the inclination angle θ are annotated for clarity.

capsule centroid. The transition of the line colours from blue to red depicts the deformation process of the capsule, transitioning from an initial spherical shape to an oval shape as it reaches the steady state. The inclination angle is defined as the angle between the longest semi-axis and the streamwise direction along the x-axis and is computed using the eigenvectors, as depicted in figure 1

$$\theta = arctan\left(\frac{\tilde{v}_y}{\tilde{v}_x}\right). \tag{2.8}$$

The bulk excess stress of the capsule suspension can be estimated using Batchelor's formulation (Batchelor 1970), considering two contributions to the total excess stress: Σ^p and Σ^f. The particle stress tensor, which depends on the interaction between capsules Σ^p, can be computed by incorporating the viscosity ratio and the Lagrangian nodal forces acting on the capsule surface, as described in the methodologies by Krüger (2012) and Gross et al. (2014)

$$\tilde{\Sigma}^p_{\alpha\beta} = -\frac{1}{\tilde{V}} \sum_{i=1}^{N} \sum_{j}^{N_{ele}} \frac{1}{2}\left(\tilde{F}^{i,j}_\alpha \tilde{r}^{i,j}_\beta + \tilde{F}^{i,j}_\beta \tilde{r}^{i,j}_\alpha\right) + \frac{1}{\tilde{V}} \sum_{i=1}^{N} \oint_{\tilde{A}_i}\left(\tilde{\lambda}_v - 1\right)\tilde{\mu}_0\left(\tilde{u}_\alpha n_\beta + \tilde{u}_\beta n_\alpha\right) \mathrm{d}\mathcal{A}, \tag{2.9}$$

where α and β are indices referring to the Cartesian directions (x, y or z), N denotes the number of capsules considered in the control volume $\tilde{V}$ and N_{ele} is the number of triangular elements on the capsule; $\tilde{\mathcal{A}}_i$ is the area of the capsule i and $\tilde{\mathcal{A}}_0$ is the surface area of the initial spherical capsule; $\tilde{F}^{i,j}$ is Lagrangian force on the node with position vector $\tilde{r}^{i,j}$. In the inertial regime, an additional Reynolds-stress-like term, denoted as Σ^f, needs to be considered to account for the contribution of flow fluctuations to the bulk stress. For a dilute system, the following formulation can be applied (Raja et al. 2010; Srivastava et al. 2016; Mwasame et al. 2017):

$$\tilde{\Sigma}^f_{\alpha\beta} = -\frac{1}{\tilde{V}} \int_{\tilde{V}} \tilde{\rho}\tilde{u}'_\alpha \tilde{u}'_\beta, \mathrm{d}V, \tag{2.10}$$

where $\tilde{u}' = \tilde{u} - \overline{\tilde{u}}$ is the flow fluctuation relative to the reference (or undisturbed) velocity of the imposed shear flow $\overline{\tilde{u}} = \tilde{\dot{\gamma}}\tilde{y}$.

The rheology of the suspension is assessed using the relative viscosity and the normal stress differences. For example, the relative viscosity of the suspension is defined as

$$\mu_r = 1 + \Sigma^{tot}_{xy} = 1 + \frac{\tilde{\Sigma}^p_{xy} + \tilde{\Sigma}^f_{xy}}{\tilde{\mu}_0\tilde{\dot{\gamma}}}, \tag{2.11}$$

where Σ_{xy}^{tot} denotes the dimensionless total excess particle shear stress. The dimensionless first and second normal stress differences are defined as

$$N_1^* = \frac{\tilde{N}_1^*}{\tilde{\mu}_0 \tilde{\gamma}} = \frac{\tilde{\Sigma}_{xx}^* - \tilde{\Sigma}_{yy}^*}{\tilde{\mu}_0 \tilde{\gamma}}, \quad N_2^* = \frac{\tilde{N}_2^*}{\tilde{\mu}_0 \tilde{\gamma}} = \frac{\tilde{\Sigma}_{yy}^* - \tilde{\Sigma}_{zz}^*}{\tilde{\mu}_0 \tilde{\gamma}}, \tag{2.12}$$

where $*$ indicates the contribution to the particle stress that arises from viscosity ratio and particle interaction (p) or from the flow fluctuation (f). Similar approaches are applied to non-dimensionalise other quantities using components of the stress tensor.

In addition to suspension rheology, we also investigate particle lateral migration by analysing the statistical motion of the capsules, which can be described using the mean-square displacement (MSD)

$$\left\langle \Delta_\psi(t)^2 \right\rangle := \left\langle \left(\tilde{X}_{i,\psi}\left(\tilde{t} + \Delta \tilde{t} \right) - \tilde{X}_{i,\psi}(\tilde{t}) \right)^2 \right\rangle_{i,t}, \tag{2.13}$$

where X denotes the position of the capsule centroid and ψ is the diffusion direction of the capsule centroid, i.e. the velocity gradient direction (y-axis) or the vorticity direction (z-axis) in the shear flow. The ensemble average is taken over time and over all freely moving capsules in the bulk flow, ensuring that both $\tilde{t}$ and $\tilde{t} + \Delta \tilde{t}$ are within the steady-state interval. Then, the diffusivity along ψ direction can be defined as the slope of the temporal evolution of the MSD in the diffusion regime. Conventionally, the dimensionless diffusivity of the capsules is scaled as

$$D_\psi = \frac{\tilde{D}_\psi}{\tilde{\gamma} \tilde{r}_0^2}, \quad \text{with} \quad \tilde{D}_\psi = \frac{\left\langle \Delta_\psi(t)^2 \right\rangle}{\tilde{d}_0^2 \tilde{\gamma} \tilde{t}}. \tag{2.14}$$

It is important to note that $\Delta \tilde{t}$ here represents a time window used for the computation of the MSD and D_ψ. This time window is distinct from, and can be significantly larger than, the numerical time step.

3. Numerical set-up

3.1. *Numerical set-up of a single capsule*

As depicted in figure 2, we consider a simple shear flow along the x axis characterised by a reference velocity $\tilde{U}_0$ within a cubic domain $\tilde{\mathcal{D}}$ with an edge length $\tilde{L}$ and centred at $(0, 0, 0)$. The boundaries of the cubic computational domain are referred to as left and right in the x direction, top and bottom in the y direction and front and back in the z direction, collectively denoted as $\partial \tilde{\mathcal{D}} = \text{left} \cup \text{right} \cup \text{top} \cup \text{bottom} \cup \text{front} \cup \text{back}$. The flow velocity $\tilde{u}$ satisfies homogeneous Dirichlet boundary conditions on the top and bottom boundaries, and periodic boundary conditions on the left/right (along x-axis) and front/back (along z-axis) boundaries. The complete set of boundary and initial conditions is as follows:

$$\tilde{u}(\tilde{x}, \tilde{t}) = \left(\frac{\tilde{U}_0}{2}, 0, 0 \right) \quad \text{on the top boundary}, \tag{3.1}$$

$$\tilde{u}(\tilde{x}, \tilde{t}) = \left(-\frac{\tilde{U}_0}{2}, 0, 0 \right) \quad \text{on the bottom boundary}, \tag{3.2}$$

$$\tilde{u}(\tilde{x}, 0) = \left(\frac{\tilde{U}_0}{\tilde{L}} \tilde{y}, 0, 0 \right) \quad \text{in} \quad \tilde{\mathcal{D}}. \tag{3.3}$$
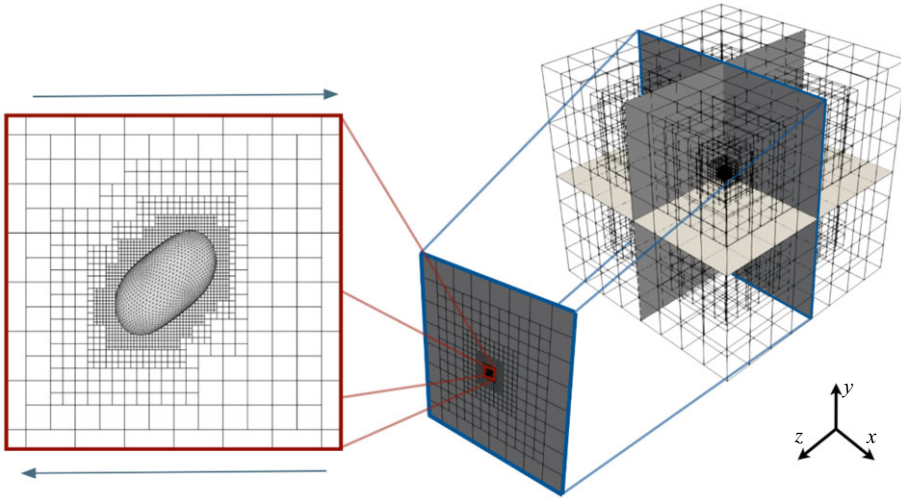
Figure 2. Illustration of a single capsule within an octree grid in a three-dimensional cubic computational domain $\tilde{\mathcal{D}}$. The red box shows a zoomed view of the capsule at $\phi = 8 \times 10^{-4}$ in simple shear flow. The blue box indicates the position of the capsule with the adaptive grid in the $x-y$ cut plane at $z = 0$.

We begin with the numerical simulation of a single elastic capsule at $0.01 \leqslant Ca \leqslant 1.0$. The capsule is strategically positioned at the centre of the cubic domain $\tilde{\mathcal{D}}$, as shown in figure 2. This set-up provides a sufficiently large domain for the accurate resolution of the flow dynamics and flow–capsule interactions. Initially at rest, the capsule at $t = 0$ is subject to a simple shear flow in both the quasi-non- to low inertial regime ($\mathcal{R}e = 0.1, 1$), hereafter called the non-inertial regime for simplicity, and the inertial regime ($\mathcal{R}e = 10, 20$). Several viscosity ratios are considered: $0.1 \leqslant \lambda \leqslant 10$ across the capsule membrane.

To achieve better accuracy in modelling capsule deformation while maintaining reasonable computational cost, we apply an octree adaptive mesh refinement. This strategy, implemented in the open-source platform Basilisk (Popinet 2015), involves partitioning a parent cube cell into eight sub-cubes for local mesh refinement in specific regions of interest (Huet & Wachs 2023). At each time step, the Cartesian octree grid is dynamically adapted: it is refined in regions with strong gradient variations in any field of interest and coarsened in regions with weak gradient variations. The primary field of interest in this study is the flow velocity. We ensure that the region near the capsule surface always has the finest grid resolution, guaranteeing that the stencils of the Lagrangian points on the capsule membrane are correctly resolved, which is crucial for the effective functioning of the immersed boundary method (IBM) (Appendix A). The hierarchical grid is constructed so that the cell size between two successive levels differs by a factor of two. Consequently, the smallest cell size is $\tilde{\Delta} = \tilde{L}/2^{n_E}$, where n_E denotes the maximum refinement level of the Eulerian octree grid. In figure 2, the locally refined grid around the capsule is highlighted. The blue box shows a cut plane at $z = 0$ across the capsule centroid, revealing the instantaneous particle position in the grid and illustrating the size difference between the particle and the computational domain. We conducted 128 simulations of a single capsule in shear flow, varying $\mathcal{R}e$, Ca and λ as depicted in table 1. Each simulation was run until a steady state of deformation and dynamics was reached, for a minimum duration.

3.2. *Flow configuration of a capsule suspension*

Based on the knowledge gained from simulating a single capsule in shear flow, we extend our simulations to investigate capsule suspensions with volume fractions ranging from
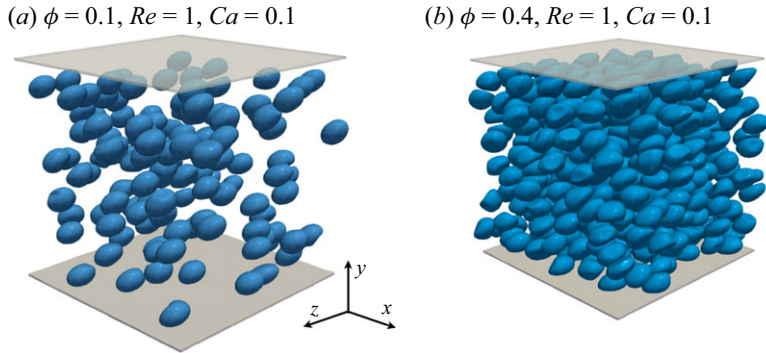
1010 A52-8

(*a*) $\phi = 0.1$, $Re = 1$, $Ca = 0.1$　　　(*b*) $\phi = 0.4$, $Re = 1$, $Ca = 0.1$

Figure 3. Illustration of the capsule suspension in a simple shear flow with increasing volume fractions (*a*) $\phi = 0.1$, (*b*) $\phi = 0.4$ in the three-dimensional cubic computational domain $\tilde{\mathcal{D}}$ with the upper and lower wall along the y-axis depicted. The periodic boundary conditions are applied along the x and z directions.

$\phi = 0.1$ to $\phi = 0.4$. Again, both the non-inertial regime ($\mathcal{R}e = 0.1$, 1) and inertial regime ($\mathcal{R}e = 10$, 20) are considered. Figure 3 depicts the capsule suspension in a simple shear flow at $\mathcal{R}e = 1$ and $\mathcal{C}a = 0.1$. To ensure consistent resolution across all simulations, all capsules have the same diameter and resolution as in the single capsule case, with a number of points per diameter of the initial spherical capsule $2\tilde{r}_0/\tilde{\Delta} = 30$. The increase in volume fraction is achieved by adding more capsules to the computational domain. Please note that in the simulation of capsule suspensions, the high number of capsules in the computational domain can significantly increase the computational cost, especially when using octree adaptive mesh refinement. This is due to the extensive refinement required around each capsule at every time step. To manage this computational expense effectively, we employ a uniform Cartesian grid for the simulation of all capsule suspensions presented in this work. This approach balances the need for spatial resolution and computational efficiency, ensuring that the simulations remain feasible without compromising accuracy. Figures 3(*a*) and 3(*b*) show capsule suspensions at $\phi = 0.1$ and $\phi = 0.4$, respectively. They clearly illustrate that, as the capsule volume fraction increases, the frequency of strong short-range capsule interactions (in the sense of capsules being in close proximity) rises markedly. To gain a comprehensive understanding of the dynamics, rheology and diffusion of the capsule suspension, we conducted more than 355 numerical simulations with varying $\mathcal{R}e$, $\mathcal{C}a$, ϕ and λ. Each simulation utilised 64 processors and ran for approximately 21 days to achieve a steady state of average deformation and dynamics, extending up to $t = 200$. For capsule diffusion, specific cases were designed with smaller time steps and longer simulation times to accurately capture the diffusion coefficient and identify the critical $\mathcal{R}e$ for regime transitions.

We thoroughly validated our solver by examining the deformation factor, semi-axis lengths, particle shear stress and the first/second normal stress differences. All our results are consistent with data reported in the literature (Bagchi & Kalluri 2010; Aouane *et al.* 2021; Guglietta *et al.* 2023). Notably, a mesh refinement test in figure 18(*g–h*) indicates that our choice of smaller grid size enhances the accuracy of numerical results compared with existing literature. For brevity, the detailed numerical validation of our solver for a single capsule and capsule suspensions in the shear flow is provided in Appendix B. In line with methodologies used in previous studies (Aouane *et al.* 2021; Guglietta *et al.* 2023), a repulsive force is also introduced when the Lagrangian nodes of adjacent capsules are in close proximity. For more details, please refer to Appendix C.
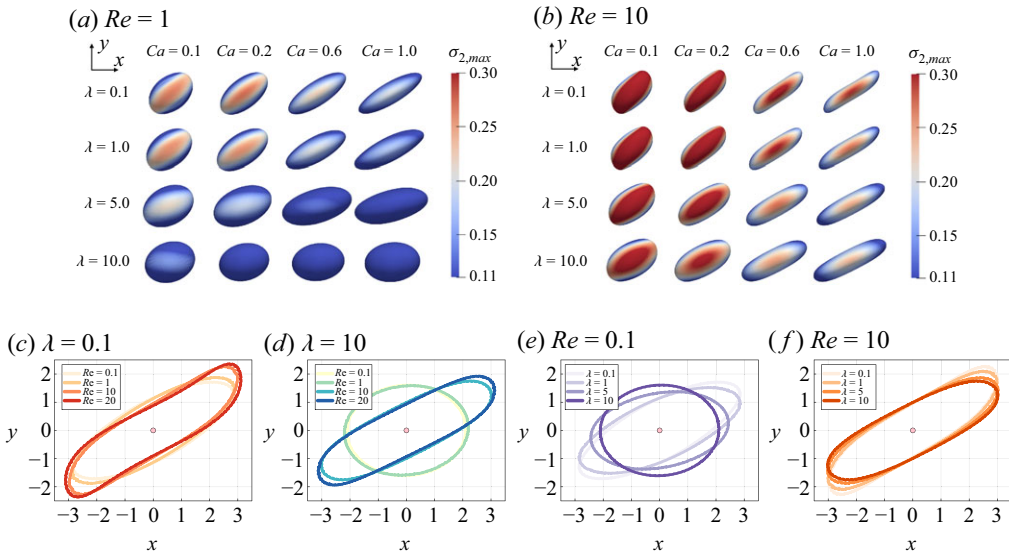
Figure 4. Deformation of capsules in the simple shear flow on the $x-y$ plane across the capsule centroid in the cases (*a*) $\mathcal{Re} = 1$ and (*b*) $\mathcal{Re} = 10$. The capsules are coloured with the maximum elastic stress $\sigma_{2,max}$ on its surface when the flow is fully developed. Capsule outlines on the cut plane $x-y$ across the capsule centroid highlighted with pink dot showing (*c–d*) effects of $\mathcal{Re}$ on the capsules at $\lambda = 0.1$ and 1; (*e–f*) effects of λ on the capsules at $\mathcal{Re} = 0.1$ and 10.

4. Single capsule results

In this section, we delve into the effects of flow inertia on the deformation, dynamics and particle stress of a single elastic capsule in the simple shear flow. We aim to provide a comprehensive understanding of how flow inertia influences capsule behaviour in different flow conditions and to shed light on the interplay between these parameters.

4.1. *Inertial effects on capsule deformation*

We first examine the deformation of a single capsule within the shear plane ($x-y$ plane) across the capsule centroid, as depicted in figure 4. Understanding the capsule deformation is critical for determining its mechanical response in the shear flow. The maximum stress experienced by the capsule is of particular interest to experimentalists, as it can be used to predict *a priori* whether a capsule will undergo plastic deformation or even break up in the flow (Häner *et al.* 2021). Specifically, the largest eigenvalue of the membrane elastic stress tensor σ_2 provides crucial insight into the membrane integrity.

In figures 4(*a*) and 4(*b*), we elucidate the impact of flow inertia ($\mathcal{Re}$), membrane elasticity ($\mathcal{Ca}$) and viscosity ratio (λ) on capsule deformation and the maximum stress distribution. To facilitate comparison, we present the outlines of the most deformable capsule ($\mathcal{Ca} = 1$) projected on the $x-y$ cut plane across the capsule centroid in figure 4(*c–f*). At $\mathcal{Ca} \leqslant 0.1$, the deformation due to high inertia is not markedly visible. However, a significant increase of the maximum stress, $\sigma_{2,max}$ with $\mathcal{Re}$, is observed. For all capsules featured in figure 4, $\sigma_{2,max}$ consistently manifests at the centre of the membrane on the $x-y$ plane, at the capsule extreme along the z-axis. An increase in $\mathcal{Ca}$ results in a relaxation of $\sigma_{2,max}$ as the capsule membrane becomes more deformable.

The capsule exhibits clearly increased elongation when flow inertia is increased in figure 4(*c–d*). Conversely, the increase of λ acts to preserve the spherical shape of
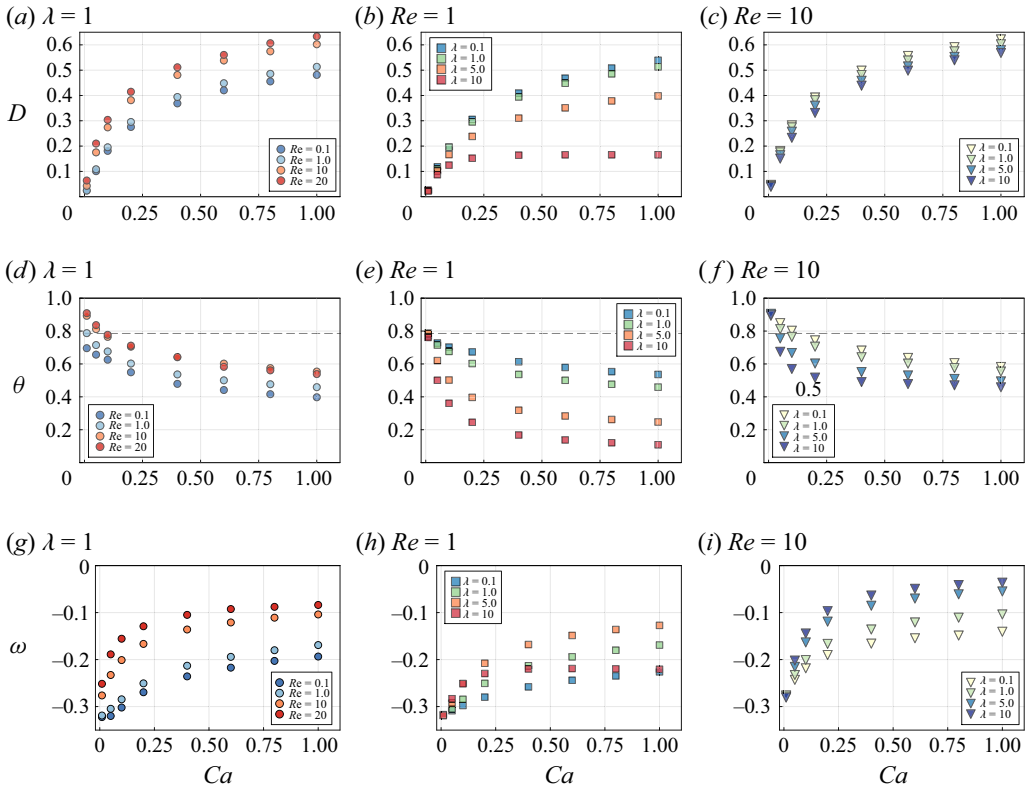
Figure 5. Effects of flow inertia on the deformation of a single capsule in a shear flow at $\mathcal{Re} = 0.1 \sim 20$, and $\lambda = 0.1 \sim 10$. (*a–c*) Evolution of the Taylor deformation factor D as a function of $\mathcal{Ca}$. (*d–f*) Evolution of the inclination angle θ in the $x-y$ shear plane as a function of $\mathcal{Ca}$, with black dashed lines denoting $\theta = \pi/4$. (*g–i*) Capsule angular velocity of tank treading, ω.

the capsule as a result of the internal resistance to deformation, especially at $\mathcal{Re} \leqslant 1$. Illustrated in figures 4(*a*) and 4(*e*), the capsule at $\mathcal{Ca} = 1$ and $\lambda = 0.1$ adopts a spindle shape, gradually transitioning to a more blunt and oval shape with increasing λ, eventually achieving an inclined oblate spheroid shape at $\lambda = 10$. In the inertial regime, depicted at $\mathcal{Re} = 10$ in figures 4(*b*) and 4(*f*), the influence of λ on capsule morphology becomes notably less pronounced, where the outlines of the capsules tend to overlap.

4.1.1. *Capsule deformation and inclination angle*

Figure 5 shows the impact of flow inertia and viscosity ratio on capsule deformation as a function of $\mathcal{Ca}$. As depicted in figure 5(*a*), one immediate effect of inertia is the enhancement of the Taylor deformation factor D, which increases with $\mathcal{Re}$ across the range of $\mathcal{Ca}$ values explored. For capsules at $\mathcal{Ca} \geqslant 0.1$, elevating the flow inertia from $\mathcal{Re} = 0.1$ to $\mathcal{Re} = 20$ leads to a consistent increase in the deformation factor, with an increment of $\Delta D \approx 0.15$. From another point of view, we fix $\mathcal{Re}$ to reveal the effects of λ on the capsule deformation in the non-inertial flow at $\mathcal{Re} = 1$ in figure 5(*b*) and the inertial flow at $\mathcal{Re} = 10$ in figure 5(*c*). In the non-inertial regime, the resistance to deformation becomes more pronounced as $\mathcal{Ca}$ increases. For example, at $\mathcal{Re} = 1$ and $\mathcal{Ca} = 1$, the deformation factor drops from $D = 0.54$ at $\lambda = 0.1$ to $D = 0.17$ at $\lambda = 10$ in figure 5(*b*). However, the impact of λ is much less pronounced in the inertial regime in

figure 5(*c*). A plausible explanation is that in the non-inertial regime (low $\mathcal{R}e$), the flow is dominated by viscous forces. At high $\mathcal{R}e$, the inertial forces exert such a strong influence on the capsule deformation that the internal viscosity becomes a secondary factor, leading to only slight changes in D. Additionally, the evolution of capsule surface area $\mathcal{A}$ closely mirrors the behaviour of the deformation parameter D under the influence of both $\mathcal{R}e$ and λ. At $\mathcal{C}a = 1$ and $\mathcal{R}e = 20$, $\mathcal{A}$ reaches a maximum value approximately 30 % larger than the initial surface area of the capsule.

In terms of the inclination angle, θ exhibits a higher value for less deformable capsules (low $\mathcal{C}a$). We see from figure 5(*d*) that increasing the flow inertia from $\mathcal{R}e = 0.1$ to $\mathcal{R}e = 10$ increases the inclination angle for all $\mathcal{C}a$ values at $\lambda = 1$. Capsules with $\mathcal{C}a \geqslant 0.2$ exhibit inclination angles $\theta < \pi/4$ (extensional axis of shear), indicating that more deformable capsules preferentially elongate along the streamwise direction. For low $\mathcal{C}a$, the increased flow inertia raises θ above $\pi/4$, consistent with observations for a single droplet in shear flow (Li & Sarkar 2005*a*; Srivastava *et al.* 2016). A maximal $\theta \approx 0.9$ is observed at $\mathcal{C}a = 0.01$, which significantly affects the interfacial stresses. At $\mathcal{R}e = 20$, θ is very close to the case at $\mathcal{R}e = 10$, indicating that the increase in θ due to inertia saturates. Similar to the deformation factor D, the increase of λ tends to decrease the inclination angle θ for all $\mathcal{C}a$ simulated, as shown in figure 5(*e–f*). Higher inertia impedes the alignment of the capsule with the flow direction, increasing θ. Conversely, increasing the viscosity ratio λ reduces θ and enhances the alignment of the capsule with the shear flow. This behaviour highlights the interplay between flow inertia and viscosity ratio in determining capsule orientation, which in turn influences the characteristics of normal stress differences – a topic we will explore further in the following discussion.

In a fully developed shear flow, the capsule exhibits a tank-treading motion, with the angular velocity ω decreasing as $\mathcal{C}a$ increases. Here, ω is defined as the time-averaged value across all surface Lagrangian points, after the flow has achieved a fully developed state. Figure 5(*g*) shows that the increase of $\mathcal{R}e$ impedes the tank-treading velocity, leading to a smaller magnitude of ω (note that the sign of ω is determined by the shear flow direction and the chosen coordinate system). This deceleration is primarily due to the capsule being stretched and elongated by inertial forces, which impedes capsule rotation. Similarly, the viscosity ratio λ also contributes to slowing down the angular velocity of the tank treading, as shown in figure 5(*h–i*). A higher λ means greater internal viscosity, which resists the internal circulation of the fluid within the capsule. An exception is noted at $\mathcal{R}e = 1$ and $\lambda = 10$ in figure 5(*h*), where the angular velocity is increased compared with the case at $\lambda = 5$ for $\mathcal{C}a \geqslant 0.2$. This behaviour can be attributed to the very high internal viscosity ($\lambda = 10$) providing sufficient resistance to prevent excessive stretching, allowing the capsule to maintain a higher rotational speed at $\mathcal{R}e = 1$. At $\mathcal{R}e = 10$, the acceleration effect observed at $\lambda = 10$ is no longer present in figure 5(*i*).
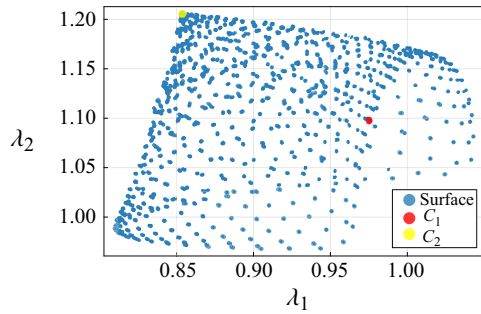
4.1.2. *Surface principal stretches*

To gain deeper insights into the deformation of the membrane and capsule dynamics, we explore the evolution of the principal stretches of the elastic membrane, denoted as λ_1 and λ_2, presented in figure 6. We focus on two specific regions on the capsule surface that undergo significant deformation. The first point, $\mathcal{C}_1$, is located on the capsule outline in the shear $x-y$ plane initially located at $(x, y, z) = (-1, 0, 0)$. The second point, $\mathcal{C}_2$, is found at an extreme of the capsule initially at $(x, y, z) = (0, 0, 1)$, where the membrane elastic
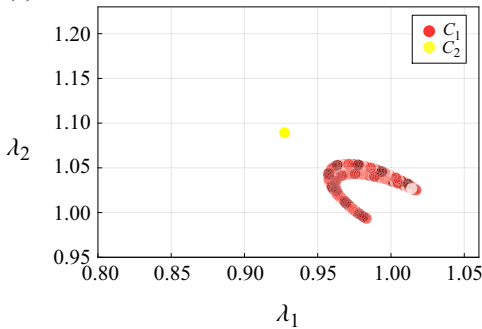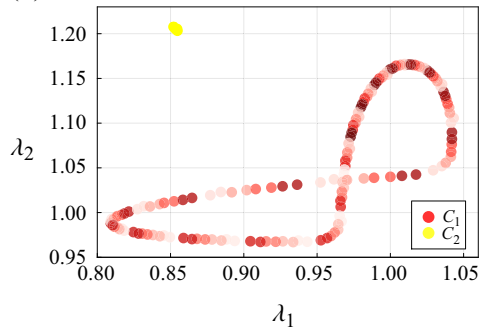
(*a*) Two critical surface points C_1 and C_2
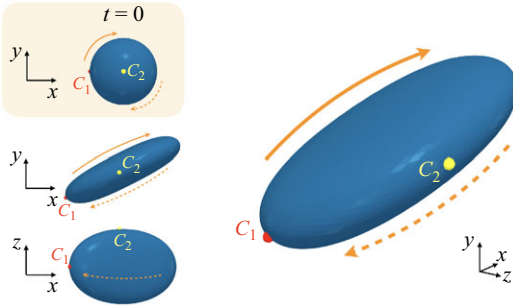
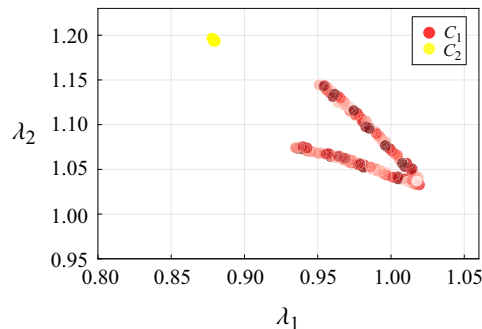(*b*) $\lambda = 10$, $Re = 1$, $Ca = 1.0$

(*c*) $\lambda = 10$, $Re = 1$, $Ca = 0.1$

(*d*) $\lambda = 10$, $Re = 1$, $Ca = 1.0$

(*e*) $\lambda = 1$, $Re = 10$, $Ca = 0.1$

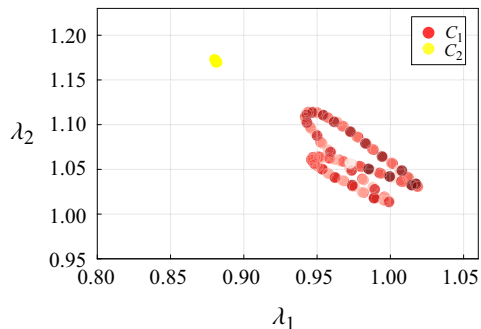(*f*) $\lambda = 10$, $Re = 10$, $Ca = 0.1$

Figure 6. Evolution of principal stretches (λ_1, λ_2) on the capsule surface. (*a*) Sketch of the rotating capsule with the two critical points highlighted, C_1 (●) denotes a point on the capsule outline in the shear plane $x-y$ across the capsule centroid and C_2 (●) is an extreme point along z-axis. (*b*) A snapshot of the principal stretch distribution in the $\lambda_1\lambda_2$ space (●) with the two critical points highlighted in corresponding colours. (*c*–*f*) Temporal evolution of the principal stretches on the two critical points C_1 and C_2, with red point darkness denoting the time evolution (from light to dark).

stress reaches its maximum values, as shown in figure 4. The specific locations of the two critical points are illustrated in figure 6(*a*) for a better clarity.

In figure 6(*b*), we present a snapshot at $t = 90$ that showcases the phase diagram of principal stretches, λ_1 and λ_2, on the whole membrane of a single capsule at $\lambda = 10$ and $Ca = 1.0$ in the flow at $\mathcal{R}e = 1$. The red dots (●) represent the principal stretches at the point C_1, which follow a periodic trajectory loosely resembling an infinity symbol ∞, as

depicted in figure 6(*d*). This trajectory highlights a significant variation in stretches at the point C_1, exhibiting values of $\Delta\lambda_1 \approx 0.25$ and $\Delta\lambda_2 \approx 0.2$. In contrast, the evolution of principal stretches at the point C_2 is marked by a stationary dot (•), indicating constant principal stretches throughout the simulation, as illustrated in figures 6(*b*) and 6(*d*). Point C_2 consistently shows the maximum λ_2 value (also the maximum elastic stress $\sigma_{2,max}$) during the simulation. The remaining surface points are represented by blue dots (•) in figure 6(*b*). These blue dots are positioned between the stationary yellow dot (C_2) and the dynamic trajectory of the red dots (C_1). The principal stretches at all points on the capsule surface are governed by the dynamic behaviour of the two critical points, C_1 and C_2.

To elucidate the impact of flow inertia and viscosity ratio, we examine additional cases of the trajectories of the principal stretches at critical points C_1 and C_2, as illustrated in figure 6(*c–f*). The varying brightness of the red dots, from light to dark, illustrates the temporal evolution of the principal stretches at C_1. The staggered colour darkness indicates that point C_1 follows a periodic trajectory, revealing multiple cycles of evolution of the principal stretches. A comparison of figures 6(*c*) and 6(*d*) reveals that an increase in Ca significantly broadens the range of principal stretches of both λ_1 and λ_2, indicating more pronounced deformation. Similarly, increasing Re leads to a higher maximum λ_2, from 1.09 to 1.2, as shown in figures 6(*c*) and 6(*f*). Furthermore, figures 6(*e*) and 6(*f*) show that an increase in λ results in a slight decrease in λ_2, while maintaining a similar range for λ_1.

In summary, these trajectory patterns are influenced by the interplay of the flow parameters Ca, Re and λ, which collectively dictate the deformation and dynamic behaviour of the capsule. Our analysis yields three important novel insights: (i) the trajectory of C_1 displays periodic behaviour, characterised by extensive variability and complex patterns at different Re, Ca and λ; (ii) the trajectory of C_2 remains static within the principal stretch (λ_1, λ_2) space, suggesting that the tank-treading motion of the capsule maintains stability in the examined cases; (iii) the principal stretch evolution at points C_1 and C_2 governs the capsule overall deformation, with all other surface points exhibiting principal stretches that lie strictly between those of C_1 and C_2.

4.1.3. *Correlation of the deformation factor*

Based on the previous discussion, it is clear that the capsule deformation is significantly influenced by three primary factors: flow inertia, elasticity of the capsule and viscosity ratio. A quantitative understanding of their roles is essential for optimising applications in biomedical engineering, where precise control over capsule behaviour is critical. In pursuit of this goal, we have formulated an empirical correlation to predict the capsule deformation, by incorporating Re, Ca and λ

$$\hat{D} = \underbrace{0.21(Ca)^{0.23}}_{f_1} \underbrace{\left(0.73\log(Ca) + 0.027Re\lambda^{-0.097} + 3.6\right)}_{f_2} \underbrace{\exp\left(-\frac{0.078\lambda}{\exp(0.32Re)}\right)}_{f_3}$$
$$- \underbrace{0.23Ca}_{f_4}, \tag{4.1}$$

where $\hat{D}$ denotes the predicted Taylor deformation factor. The first factor, f_1, represents the base influence of Ca, while the mixed factor, f_2, describes the combined nonlinear effects of Ca, Re and λ. Overall, the deformation $\hat{D}$ increases with higher values of both Re and Ca; λ acts as a damping factor on the deformation, with its effect being most significant at low Re and Ca, where surface elasticity and viscous resistance dominate,
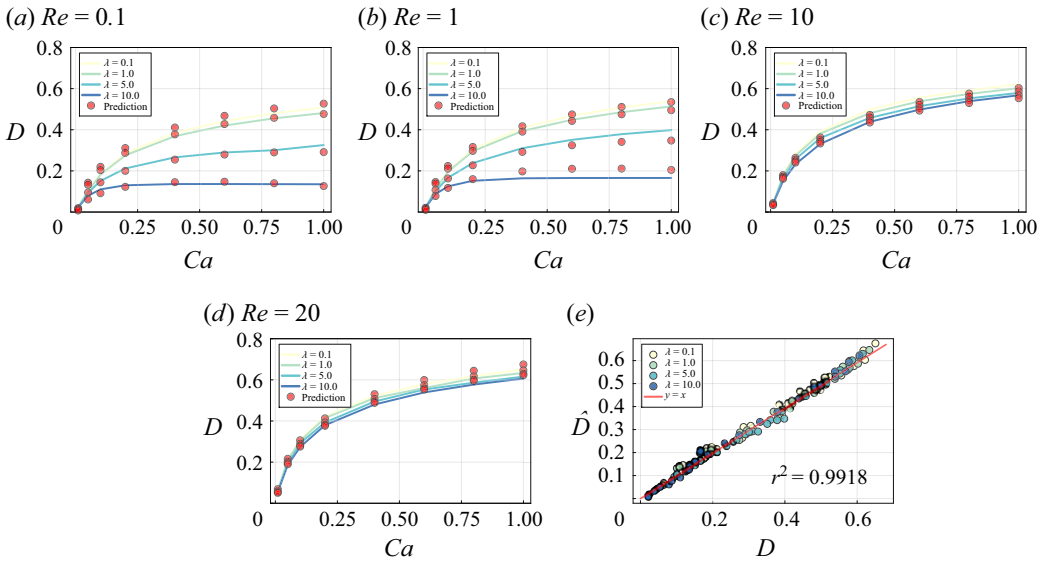
Figure 7. Correlation prediction of the Taylor deformation factor $\hat{D}$ in comparison with our computed results. (*a–d*) Evolution of D in function of $\mathcal{C}a$ at $\mathcal{R}e = 0.1 \sim 20$; (*e*) direction comparison between the prediction $\hat{D}$ and numerical results D.

limiting deformation. The exponential decay term f_3 shows that the damping effect due to λ decreases as $\mathcal{R}e$ increases, allowing more significant deformation at higher flow inertia, which captures the transition to the inertial regime. The final term f_4, which subtracts a linear function of $\mathcal{C}a$, provides a stabilising effect that adjusts the overall deformation. This empirical correlation allows us to quantify the complex interplay between fluid dynamics and material properties that govern the capsule deformation.

Figure 7(*a–d*) presents a meticulous comparison between our numerical results (obtained by high-fidelity interface-resolved simulations, illustrated with coloured lines) and the results predicted by the correlation (as formulated in (4.1) and indicated by red dots) for the evolution of D of a single capsule. The comparison reveals the remarkable accuracy of the correlation in predicting the deformation factor D across the entire range of parameter space ($\mathcal{R}e$, $\mathcal{C}a$, λ) explored. The panels distinctly illustrate the increase of D as a function of $\mathcal{R}e$, while the variations of D with respect to $\mathcal{C}a$ are also accurately reproduced. Additionally, the influence of λ on the decrease of D is comprehensively delineated in figure 7(*a–d*). In general, the correlation in (4.1) demonstrates high precision in predicting the deformation factor D as depicted in figure 7(*e*), achieving an average relative error of $\bar{\varepsilon}_r = 7.21\%$ and a determination coefficient of $r^2 = 0.9918$. This level of accuracy underscores the robustness of our empirical correlation in capturing the complex dynamics governing capsule deformation. Moreover, it serves as a valuable tool for experimentalists and engineers, providing a reliable means to estimate capsule deformation and facilitating better design of microfluidic devices.

4.2. *Inertial effects on particle stress*

In addition to capsule deformation, the particle stress exerted on the capsule membrane is also of vital importance. Understanding the behaviour of a single capsule provides valuable insights into the dynamics and rheology of suspensions of capsules. Figure 8 illustrates the evolution of particle shear stress Σ_{xy}^p, first and second normal stress
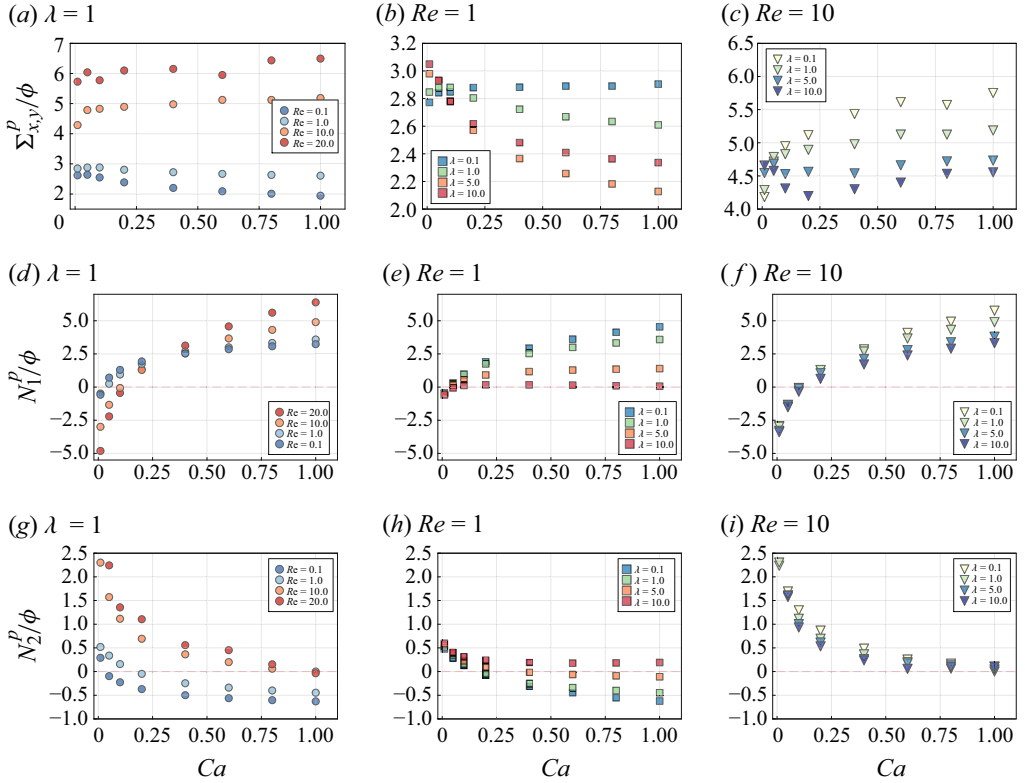
Figure 8. Effects of inertia on the particle stress of a single capsule in a shear flow at $\mathcal{R}e = 0.1 \sim 20$ and $\lambda = 0.1 \sim 10$. (*a-c*) Particle shear stress Σ^p_{xy}/ϕ, (*d-f*) first normal stress difference N^p_1/ϕ, (*g-i*) second normal stress difference N^p_2/ϕ.

differences (N^p_1, N^p_2) as a function of $\mathcal{C}a$ for a single capsule. The influence of flow fluctuations is not accounted for in this section due to the minimal volume fraction. We divide the particle stress by its volume fraction ϕ in figure 8 for a better visualisation.

From figure 8(*a*), we observe that an increase in $\mathcal{R}e$ leads to a clear rise in Σ^p_{xy}. At $\mathcal{R}e \leqslant 1$, higher $\mathcal{C}a$ values tend to reduce the shear stress, whereas for $\mathcal{R}e \geqslant 10$, $\mathcal{C}a$ has an opposite effect. This behaviour mainly results from changes in two key factors affecting Σ^p_{xy}: (*i*) the capsule elongation, which is proportional to r_1 and (*ii*) its inclination angle θ. A longer r_1 and a higher θ contribute to increase the shear stress Σ^p_{xy}. For instance, the increase in Σ^p_{xy} with $\mathcal{R}e$ in figure 8(*a*) is mainly due to the more elongated capsule at higher inertia. As the capsule deformation intensifies with increasing $\mathcal{C}a$, there is a corresponding rise in r_1, while θ undergoes a noticeable reduction. In the non-inertial regime, such as at $\mathcal{R}e = 0.1$, the increase in r_1 is modest while the effect of decreasing θ is more pronounced, leading to a decrease in shear stress with $\mathcal{C}a$ as shown in figure 8(*a*). At higher flow inertia ($\mathcal{R}e = 10$), r_1 increases more significantly ($r_1 = 2.0$ at $\mathcal{C}a = 1$), which outweighs the effect of the decreasing θ, causing shear stress to rise with $\mathcal{C}a$. The interplay of r_1 and θ becomes clearer when considering the effects of λ on the particle shear stress, as shown in figures 8(*b*) and 8(*c*). We see in figure 5 that a higher λ hinders capsule elongation, while simultaneously reducing the inclination angle θ, which results in a clear decreasing trend of Σ^p_{xy} with λ for $\mathcal{C}a \geqslant 0.1$. For capsules at $\mathcal{C}a = 0.01$

1010 A52-16

and $Ca = 0.05$, Σ_{xy}^p increases with λ due to the stronger internal viscous resistance and corresponding limited deformation.

Figure 8(*d–f*) illustrates the evolution of the first normal stress difference $N_1^p = \Sigma_{xx}^p - \Sigma_{yy}^p$ as a function of Ca at various Re and λ. In figure 8(*d*), we observe that at $Ca \leqslant 0.1$, the flow inertia tends to decrease N_1^p, while at $Ca \geqslant 0.2$, higher Re leads to an increase in N_1^p in the shear flow. These two opposing behaviours can also be explained by the interplay between capsule elongation and inclination. At low Ca, the high inclination angle θ (as depicted in figure 5*e*) promotes normal stress along the y direction Σ_{yy}^p. For the same elastic force along r_1, a larger θ results in a greater component projected onto the y-direction. Conversely, at $Ca \geqslant 0.1$, the more significant elongation of the capsule together with the smaller θ, enhances normal stress along the streamwise direction (x-axis) Σ_{xx}^p. Different from rigid particle suspensions (Haddadi & Morris 2014), the sign of N_1^p changes in the capsule suspension. This change of sign aligns closely with the variation of the capsule inclination angle θ, similar to what is observed in studies of droplet emulsions (Srivastava *et al.* 2016). We see that the reduction in θ from $\pi/4$ (extension axis of shear flow) in figure 5(*d–f*) drives the transition of N_1^p from negative to positive values for elastic capsules. For emulsions of droplets, with a constant surface tension, the stresslet term in (2.9) is purely geometric, which means that the sign change arises directly from the inclination angle exceeding $\pi/4$ (Singh *et al.* 2014). Please note that while similar mechanism applies, the sign change in N_1^p is not purely geometric for elastic capsules in figure 8(*d–f*), due to the distinct nature of their membrane. In figure 8(*e–f*), the viscosity ratio λ clearly mitigates N_1^p. Higher internal viscosity helps maintain a more balanced stress distribution between the x and y directions, thereby reducing the difference N_1^p.

Similarly, figures 8(*g–i*) depicts the evolution of the second normal stress difference ($N_2^p = \Sigma_{yy}^p - \Sigma_{zz}^p$). An increase in Re forces higher deformation in the xy plane and hence higher stress along the y-axis relative to the z-axis. Conversely, an increase in Ca leads to smaller inclination angle θ, which reduces Σ_{yy}^p and consequently decreases N_2^p, even to negative values. At $Re = 1$ in figure 8(*h*), the high internal viscosity promotes a more balanced stress distribution in the shear plane and enhances Σ_{yy}^p with respect to Σ_{zz}^p. However, λ has a very limited impact on N_2^p at $Re = 10$ in figure 8(*i*).

5. Capsule suspension results

In this section, we explore the behaviour of capsule suspensions in the shear flow. We begin by examining how flow inertia affects capsule deformation and dynamics, including microstructure and lateral diffusion of the capsule suspension. Then, we analyse the impact of inertia on the rheological properties of the suspension, by establishing a connection with the previous results of a single capsule.

5.1. *Inertial effects on capsule deformation and dynamics*

In a suspension, the interaction between capsules is the primary factor influencing its dynamics and rheological behaviour. In a very dilute system, capsules rarely encounter each other and behave similarly to single capsules in the flow. Hence, in this section, we investigate capsule suspensions with volume fractions in the range $0.1 \leqslant \phi \leqslant 0.4$ in both the non-inertial regime ($Re = 0.1, 1$) and the inertial regime ($Re = 10, 20$).

5.1.1. *Bridge structures*

We first examine the capsule interactions in dense suspensions with volume fraction of $\phi = 0.4$ at different Re and Ca in figure 9. The outlines of the capsules are projected onto

(*a*) $Re = 1$, $Ca = 0.1$ (*b*) $Re = 1$, $Ca = 1.0$ (*c*) $Re = 10$, $Ca = 0.1$ (*d*) $Re = 10$, $Ca = 1.0$

(*e*) $Re = 1$, $Ca = 0.1$ (*f*) $Re = 1$, $Ca = 1.0$ (*g*) $Re = 10$, $Ca = 0.1$ (*h*) $Re = 10$, $Ca = 1.0$
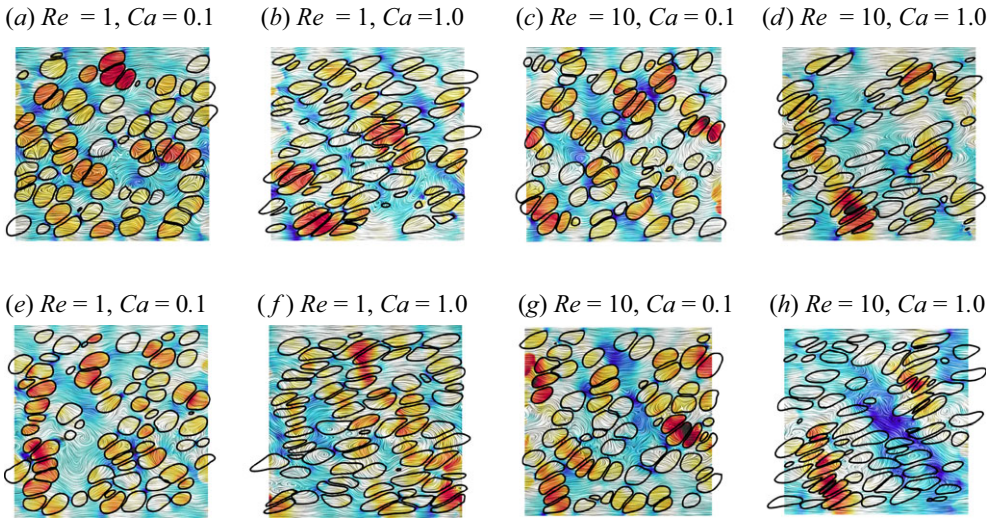

Figure 9. Snapshots of the capsule suspension at $\phi = 0.4$ projected on the shear plane $z = 0$ with the flow field coloured by the pressure distribution (red indicates regions of high pressure, while blue represents areas of low pressure) and the perturbed flow streamlines; with viscosity ratios (*a–d*) $\lambda = 1$, (*e–h*) $\lambda = 5$.

the shear plane at $z = 0$ in black contours. Additionally, figure 9 illustrates the pressure distribution in the same shear plane, with regions of low and high pressure indicated by blue and red colours, respectively. In shear flow, the streamwise velocity along the x-axis is significantly greater than its transverse and spanwise components. To better illustrate the flow dynamics, we subtract the imposed shear flow velocity from the total velocity and present the streamlines of the perturbed velocity field $\tilde{u}' = \tilde{u} - \tilde{U}_0 \tilde{y}/\tilde{L}$ in figure 9.

Figures 9(*a*) and 9(*b*) show that unsurprisingly capsules become more elongated at higher Ca. In very dilute systems, the capsules often form pairs. As ϕ increases, these pairs tend to cluster together, forming longer structures. In such regions, an intriguing bridge structure emerges, reminiscent of the rouleaux structures observed in experimental studies of Chinchilla *et al.* (2021) and Lee & Paeng (2021). The formation of the bridge structures is more prevalent at higher values of Re and Ca, as shown in figures 9(*c*) and 9(*d*). When the internal fluid viscosity is increased to $\lambda = 5$, the bridge-like structures in the flow become more prominent, as demonstrated in figures 9(*e*) to 9(*h*). It is important to note that these structures do not adhere together as real rouleaux structures would, since no adhesion model is applied to the surface of the capsules. Nonetheless, these observations provide strong evidence that pure hydrodynamic interactions can significantly contribute to the formation of rouleaux structures.

Additionally, all panels in figure 9 demonstrate a marked increase in local fluid pressure during capsule interactions, driven by compressive forces. The primary axis of the bridge structures are typically perpendicular to the extension axis of shear flow, contributing to the anisotropy of the microstructure and enhancing interactions. The anisotropy induced by bridge structures leads to a redistribution of stresses among the different directions. This impacts the particle stress tensor, altering the rheological properties of the suspension, including the first and second normal stress differences. As an additional discussion, the inhomogeneous distribution of membrane elastic stresses on the capsule surface in the bridge structure is presented and analysed in Appendix D.
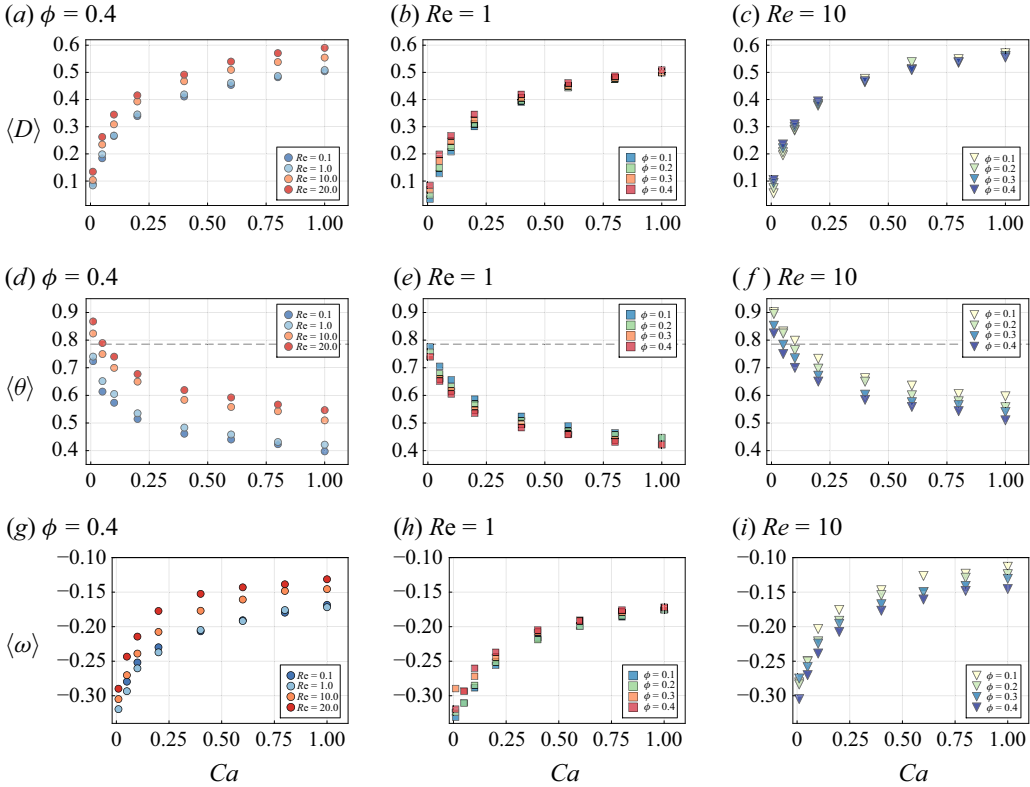
Figure 10. Effects of flow inertia on the deformation and dynamics of capsule suspensions at $\lambda = 1$, $\mathcal{R}e = 0.1 \sim 20$ and $\phi = 0.1 \sim 0.4$. (*a–c*) Ensemble-averaged Taylor deformation factor $\langle D \rangle$, with black dashed lines denoting $\theta = \pi/4$; (*d–f*) inclination angle $\langle \theta \rangle$; (*g–i*) angular velocity of tank-treading $\langle \omega \rangle$.

5.1.2. *Average deformation and inclination angle*

We then study the effects of inertia on the deformation of capsules at viscosity ratio $\lambda = 1$ in a suspension with increasing volume fraction. Simulations of suspensions with a higher viscosity ratio $\lambda = 5$ are also performed and analysed. Detailed results and discussions for these cases are provided in Appendix E. In the following, the symbol $\langle \cdot \rangle$ represents the ensemble average of physical quantities once the flow regime has fully developed, such as $\langle x \rangle := \frac{1}{N} \sum_{i=1}^{N} x_i$, with N the total number of capsules.

In figure 10, we depict the evolution of the ensemble-averaged Taylor deformation factor $\langle D \rangle$, inclination angle $\langle \theta \rangle$ and angular velocity $\langle \omega \rangle$ as a function of $\mathcal{C}a$. In general, capsules exhibit similar deformation evolution with $\mathcal{C}a$ as a single capsule in shear flow does. At $\phi = 0.4$, $\langle D \rangle$ increases with $\mathcal{C}a$ and $\mathcal{R}e$ in figure 10(*a*). At $\mathcal{R}e \leqslant 1$, the effects of flow inertia on variations of $\langle D \rangle$ are minimal, such that data points nearly overlap for $\mathcal{R}e = 0.1$ and $\mathcal{R}e = 1$ at the scale presented. Further increase of $\mathcal{R}e$ enhances the deformation factor $\langle D \rangle$ in the inertial regime. In both figures 10(*b*) and 10(*c*), the influence of ϕ on $\langle D \rangle$ is more pronounced for cases at low $\mathcal{C}a$. This is attributed to the more intense short-range capsule interactions at low $\mathcal{C}a$.

The variation of the inclination angle $\langle \theta \rangle$ at $\phi = 0.4$ is depicted in figure 10(*d*). It is clear that flow inertia generally leads to an increase in $\langle \theta \rangle$. Conversely, in figure 10(*e–f*), the decrease of $\langle \theta \rangle$ with ϕ can be attributed to the reduced free space between capsules along the y direction. Regarding the average angular velocity $\langle \omega \rangle$, an increase in $\mathcal{R}e$ leads to a
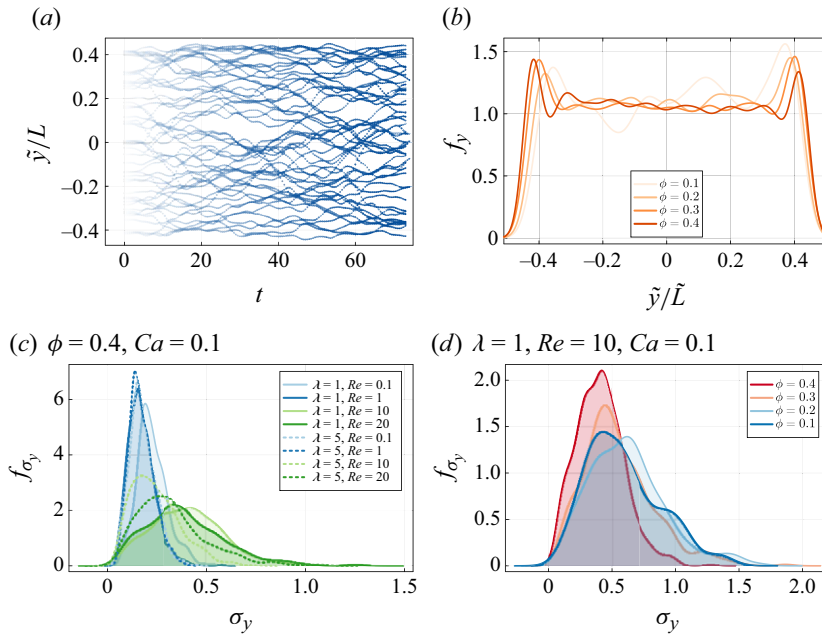
Figure 11. Evolution of the capsule suspension migration in a simple shear flow. (*a*) Temporal evolution of 50 capsule trajectories along the *y*-axis in the case of $\phi = 0.4$, $\lambda = 1$, $\mathcal{Re} = 10$, $\mathcal{Ca} = 1.0$; (*b*) probability density function (*f*, PDF) of the capsule distribution along the *y*-axis in the suspension of increasing volume fraction ϕ at $\lambda = 1$, $\mathcal{Re} = 10$ and $\mathcal{Ca} = 0.1$. (*c*, *d*) Evolution of the PDF of the standard deviation of the capsule motion along the *y*-axis under the effects of ϕ, $\mathcal{Re}$, λ and $\mathcal{Ca}$.

lower magnitude of $\langle \omega \rangle$ at $\phi = 0.4$, as seen in figure 10(*g*). In comparison with figure 5(*g*), $\langle \omega \rangle$ exhibits similar values as those of the single capsule in the non-inertial regime at $\mathcal{Re} \leqslant 1$. We observe that the impact of ϕ on $\langle \omega \rangle$ is limited at $\mathcal{Re} = 1$ in figure 10(*h*). Interestingly at $\mathcal{Re} \geqslant 10$, the angular velocity of the dense suspension is observed to exceed that of a single capsule. The increase of volume fraction enhance the particle shear stress, which in turn accelerates the tank-treading of the capsules as shown in figure 10(*i*).

5.1.3. *Lateral transport and diffusion*

We now examine the diffusion dynamics of the capsules. We focus on how the capsules migrate in the direction of the velocity gradient (along the *y*-axis) and in the spanwise direction (along the *z*-axis). To provide an intuitive illustration, we present the trajectories of 50 initially randomly distributed capsules in a suspension at $\phi = 0.4$, as shown in figure 11(*a*). This figure shows the initial positions of the 50 capsules and their trajectories along the *y*-axis over $t \in [0, 70]$ in the shear flow. It can be observed that the capsules exhibit varying patterns of migration along the *y*-axis: some oscillate within a limited region, while others migrate as far as half the computational domain over $t \in [0, 70]$. By computing the time average of the number of capsules along the *y*-axis after the flow is fully developed, we plot the probability density function (PDF) f_y of the capsule spatial distribution. Figure 11(*b*) reveals two depletion layers adjacent to the walls, with small peaks in capsule concentration at $\tilde{y}/\tilde{L} = \pm 0.4$. An increase in volume fraction ϕ appears to have only minor effects on the distribution f_y.

Additionally, we investigate how λ, $\mathcal{Re}$ and ϕ affect the standard deviation σ_y of capsule trajectory fluctuations along the *y*-axis. The corresponding PDFs, denoted f_{σ_y}, are plotted
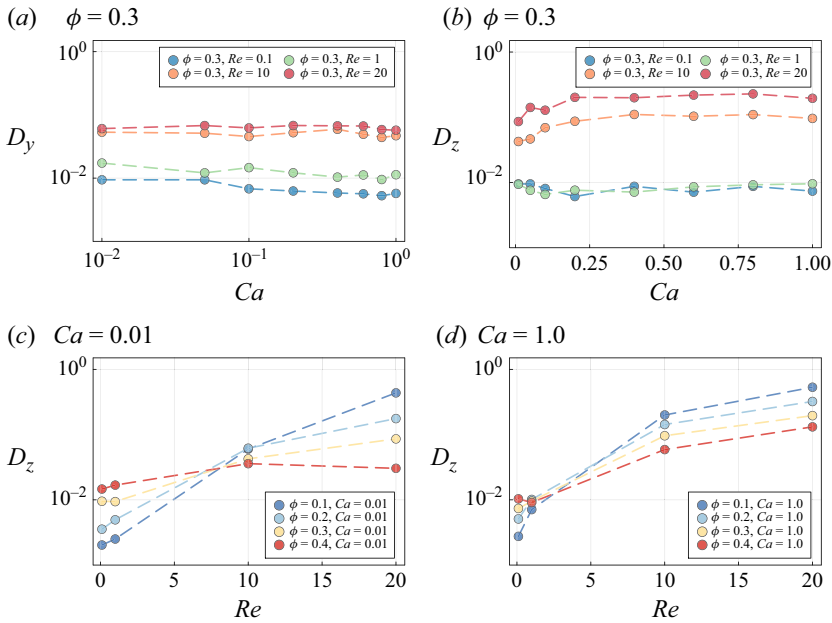
Figure 12. Diffusivity of the capsule suspension as a function of $\mathcal{C}a$ and $\mathcal{R}e$. (*a-b*) Comparison between D_y and D_z; (*c-d*) effects of flow inertia $\mathcal{R}e$ and volume fraction ϕ.

in figure 11(*c–d*). We observe that an increase in $\mathcal{R}e$ flattens f_{σ_y}, and raises $\sigma_{y,peak}$, the value of σ_y corresponding to the peak of f_{σ_y}, indicating that flow inertia enhances capsule migration. However, increasing λ has the opposite effect, reducing $\sigma_{y,peak}$, though its impact on the shape of f_{σ_y} remains minor, as shown in figure 11(*c*). Figure 11(*d*) illustrates the evolution of f_{σ_y} with increasing ϕ from 0.1 to 0.4. An increase in ϕ leads to more short-range capsule interactions and restricts the free motion of the capsules along the *y*-axis. This results in a narrower distribution and a lower $\sigma_{y,peak}$.

Subsequently, we take a closer look at capsule migration by computing the MSD using (2.13). The MSD represents the average squared distance that a particle has moved along a direction ψ over a time interval Δt. In an unsheared Brownian solid sphere system, without a suspending fluid, the MSD is quadratic ($\propto \Delta t^2$) for small Δt, known as the ballistic regime, and linear ($\propto \Delta t$) for large Δt, known as the diffusive regime. In a simple shear flow, the Brownian contributions are limited, and particle diffusion becomes primarily shear induced and anisotropic (Eckstein *et al.* 1977; Leighton & Acrivos 1987; Breedveld 2000). Since the shear rate is constant in a simple shear flow, particle diffusion is solely due to their interactions (Krüger 2012). With the presence of neighbouring particles, straight-line motion is impeded, resulting in non-affine displacement and diffusive motion. In the following, we investigate the diffusion properties of elastic capsules and reveal particular properties of the capsule diffusivity D_ψ with the increase of flow inertia and capsule volume fraction. To wall effects, we will focus mainly on the diffusion behaviour of the capsules along the *z*-axis in the suspension.

We begin by presenting the overall behaviour of capsule diffusivity D_ψ, computed using (2.14). The evolution of D_ψ along the *y*- and *z*-axes as a function of $\mathcal{C}a$ in a suspension at $\phi = 0.3$ is shown in figures 12(*a*) and 12(*b*), respectively. The high flow inertia leads to an apparent increase in diffusivity in both directions, while the effects of $\mathcal{C}a$ remain minor. Depending on the flow regime, the volume fraction ϕ has two opposite effects on the capsule diffusion. In the non-inertial regime, the increase of ϕ promotes
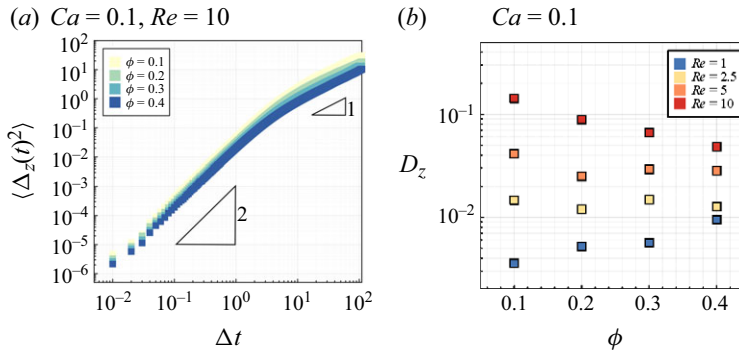
Figure 13. (*a*) Evolution of MSD of the capsule suspension for increasing ϕ; (*b*) evolution of capsule diffusivity D_z within the Reynolds number range $1 \leqslant \mathcal{R}e \leqslant 10$, showing the transition from the non-inertial to the inertial regime.

the capsule diffusion D_z in figure 12(*c*), which simply results from enhanced interactions between capsules. Conversely, at $\mathcal{R}e \geqslant 10$, D_z decreases with ϕ, indicating that a high ϕ impedes capsule diffusion along the z-axis. One possible explanation is that, at higher inertia, the streamline movement of capsules tends to dominate, reducing the influence of lateral motion, especially in more densely packed suspensions where inter-particle interactions are stronger and hinder transverse movements. A similar tendency is also observed at $\mathcal{C}a = 1.0$ in figure 12(*d*), the most deformable case in this study. There is a clear regime transition in the capsule suspension between the non-inertial regime $\mathcal{R}e = 1$ and the inertial regime $\mathcal{R}e = 10$.

Figure 13 presents the MSD along the z-axis of the capsule suspension for $1 \leqslant \mathcal{R}e \leqslant 10$ and $0.1 \leqslant \phi \leqslant 0.4$. In the $\log - \log$ plots, the MSD evolution shows a slope $\propto \Delta t^2$ in the ballistic regime and $\propto \Delta t$ in the diffusion regime, consistent with the behaviour observed in solid particle suspensions. This transition process exists across all the parameter ranges investigated. In particular, in figure 13(*a*), increasing the capsule volume fraction leads to a decrease of MSD at $\mathcal{R}e = 10$, which supports the observations of figure 12(*c*). The decrease of MSD is more pronounced in the diffusion regime than in the ballistic regime. This trend is opposite to the case at $\mathcal{R}e \leqslant 1$, confirming the existence of a transition from the non-inertial regime to the inertial regime. To better capture this novel transition process, we perform additional simulations and plot the diffusivity D_z as a function of ϕ for a capsule suspension at $\mathcal{C}a = 0.1$ in figure 13(*b*). At other values of $\mathcal{C}a$, the evolution of D_z mirrors that at $\mathcal{C}a = 0.1$, and therefore, the results are not plotted to eliminate redundancy. Figure 13(*b*) clearly shows that D_z exhibits an increasing trend with ϕ at $\mathcal{R}e = 1$, similar to the behaviour observed in solid particle suspensions. As ϕ increases, the probability of strong short-range capsule interactions rises, enhancing mixing and their lateral migration along the z-axis. Generally, increasing flow inertia leads to higher capsule diffusivity due to greater lateral motion following capsule interactions at all ϕ levels. The enhancement of lateral motion by $\mathcal{R}e$ along the z-axis is more evident at low volume fractions (e.g. $\phi = 0.1$). However, a further increase in ϕ impedes the lateral motion of capsules, as the probability of encountering a neighbouring capsule with opposite lateral motion rises. Thus, the steric interactions between neighbouring capsules result in a decrease in D_z with ϕ, which is observed for $\mathcal{R}e \geqslant 5$ in figure 13(*b*). At $\mathcal{R}e = 2.5$ the capsule diffusivity exhibits similar values across the range $\phi = 0.1$ to 0.4. Based on the current dataset, the critical $\mathcal{R}e_c$ for the non-inertial regime to inertial regime transition is identified to be between $\mathcal{R}e = 1$ and $\mathcal{R}e = 2.5$.
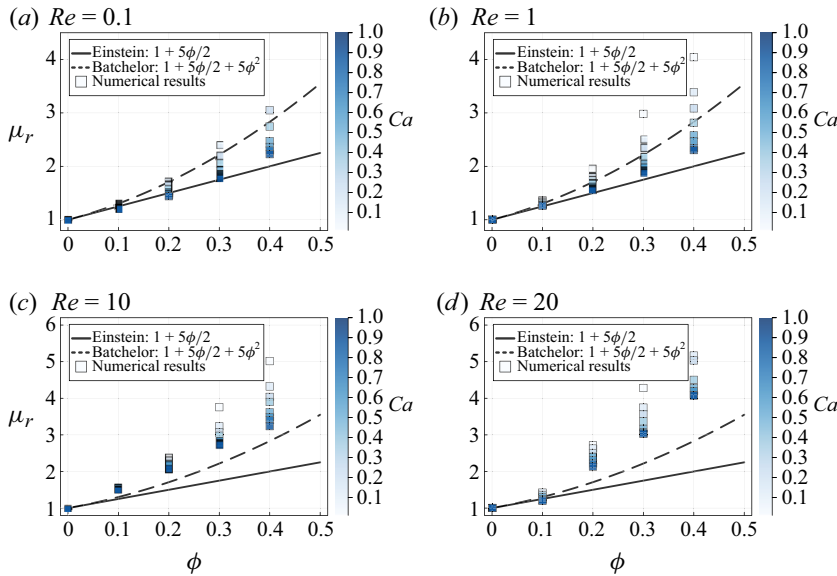
1010 A52-22

Figure 14. Relative viscosity μ_r of the capsule suspension as a function of ϕ. Einstein's correlation is shown as a solid black line, Batchelor's as a black dashed line and the effects of $\mathcal{Ca}$ are illustrated from light blue (low $\mathcal{Ca}$) to dark blue (high $\mathcal{Ca}$).

Additionally, knowing that in the absence of capsule interactions, a single capsule at steady state exhibits little lateral motion. It is presumed that there exists a critical volume fraction ($\phi_c \leqslant 0.1$) at which D_z reaches its maximum value for the suspension at $\mathcal{Re} = 10$, before it decreases as depicted in figure 13(*b*).

5.2. *Inertial effects on suspension rheology*

Building on the insights gained from the deformation and diffusion of capsule suspensions, we now investigate the effects of flow inertia on their rheology. We begin by examining the relative viscosity, followed by an analysis of the normal stresses.

5.2.1. *Relative viscosity*

Figure 14 shows the evolution of relative viscosity defined in (2.11) as a function of ϕ at $0.1 \leqslant \mathcal{Re} \leqslant 20$. The simulation results for capsule suspension, at $0.01 \leqslant \mathcal{Ca} \leqslant 1.0$, are depicted using colours from light to dark blue. In figure 14(*a*), it is clear that most data points at $\mathcal{Re} = 0.1$ lie between the correlations of Einstein (1911) and Batchelor & Green (1972). Einstein's equation is a simple model for predicting the relative viscosity of a dilute suspension of non-interacting, rigid spherical particles. It assumes that the particle concentration is very low, so interactions between particles are negligible. Batchelor's equation includes a quadratic term to account for hydrodynamic interactions and Brownian motion in a more concentrated suspension. We observe that less deformable capsules (at low $\mathcal{Ca}$) exhibit relative viscosities close to Batchelor's correlation. As the deformability of the capsule increases (at a higher $\mathcal{Ca}$) the value of μ_r tends to decrease for all volume fractions investigated ($0.1 \leqslant \phi \leqslant 0.4$). One possible reason is that more deformable capsules experience reduced hydrodynamic interactions because they can adapt to the flow and align more smoothly with the fluid streamlines, thus reducing μ_r. As $\mathcal{Re}$ increases, we have higher μ_r especially at small $\mathcal{Ca}$. In figure 14(*b*), the relative viscosity μ_r of the suspension at $\mathcal{Ca} \leqslant 0.2$ largely exceeds the values predicted by Batchelor's correlation.

In the inertial regime, at $\mathcal{Re} \geqslant 10$, the values of μ_r further increase, and both correlations fail to capture the numerical data of $\phi \geqslant 0.2$ in figure 14(c–d).

Considering flow inertia is necessary for more accurate predictions and better control over the rheological properties of capsule suspensions within our parameter space. In the following, we establish several new correlations to better predict the relative viscosity μ_r of the capsule suspension in the inertial regime. We first extend Batchelor's correlation and propose the following empirical correlation based on the entire numerical dataset within the parameter space $0.1 \leqslant \phi \leqslant 0.4$, $0.1 \leqslant \mathcal{Re} \leqslant 20$ and $0.01 \leqslant \mathcal{Ca} \leqslant 1.0$ using a multivariate regression

$$\mu_r = 1.34 - 6.68\phi + \left(-0.23 + 11.13\phi^{1.19}\right)\mathcal{Ca}^{-0.066}\left(1 + 0.081\mathcal{Re}^{0.62}\right). \quad (5.1)$$

Instead of a simple quadratic term, our multivariate correlation explicitly incorporates the two additional variables $\mathcal{Ca}$ and $\mathcal{Re}$ to account for capsule deformability and flow inertia, respectively. The correlation shows good agreement with our computed results, accurately capturing the increasing trend of μ_r with ϕ and the decreasing trend with $\mathcal{Ca}$. Although there exist a few discrepancies at low $\mathcal{Ca}$ and low $\mathcal{Re}$, the model demonstrates an average relative error $\langle\epsilon\rangle = 4.9\,\%$ and a determination coefficient of $r^2 = 0.9916$.

A second way to predict the relative viscosity of the capsule suspension is to incorporate the deformability of the capsules into the volume fraction ϕ and apply an Eilers-type model (Aouane *et al.* 2021)

$$\mu_r = \left(1 + \frac{\alpha\phi_e}{1 - \beta\phi_e}\right)^2, \quad (5.2)$$

where α and β are coefficients of the model, and ϕ_e denotes the effective volume fraction of the capsule suspension. In the non-inertial regime, Rosti *et al.* (2018) proposed the following effective volume fraction, considering an effective sphere:

$$\phi_{e,\,Rosti} = \frac{4}{3}\pi\langle r_3\rangle^3\frac{N}{V}. \quad (5.3)$$

However, this definition is not well suited for elongated capsules in inertial flow, especially for $\mathcal{Re} \geqslant 10$. Therefore, we propose a novel alternative definition of the effective volume fraction, considering an effective spheroid

$$\phi_e = \frac{4}{3}\pi\langle r_1\rangle\langle r_3\rangle^2\frac{N}{V}. \quad (5.4)$$

This definition emphasises the role of particle elongation under flow inertia and proves to be more effective for the parameter space investigated, particularly for capsules in inertial flow. The following analysis is based on the novel spheroidal effective volume fraction defined by (5.4).

In figure 15, we present the relative viscosity μ_r of the capsule suspension as a function of the effective volume fraction ϕ_e for $0.1 \leqslant \mathcal{Re} \leqslant 20$. To enhance clarity, we show the cases separately at different $\mathcal{Re}$ in the panels. For a single capsule in the shear flow, we have $\mu_r = 1$ as $\phi_e \to 0$. In the non-inertial regime, at $\mathcal{Re} \leqslant 1$, the values of μ_r collapses to a master curve as a function of ϕ_e, as shown in figure 15(a–b). In the inertial regime, the influence of $\mathcal{Ca}$ on μ_r becomes more pronounced, as illustrated in figure 15(c). Although the numerical results still approximate a master curve, the data points are grouped by ϕ and show more outliers at small $\mathcal{Ca}$. Consistent with the lateral migration of capsules discussed above, the behaviour of the capsule suspension in the inertial regime differs from
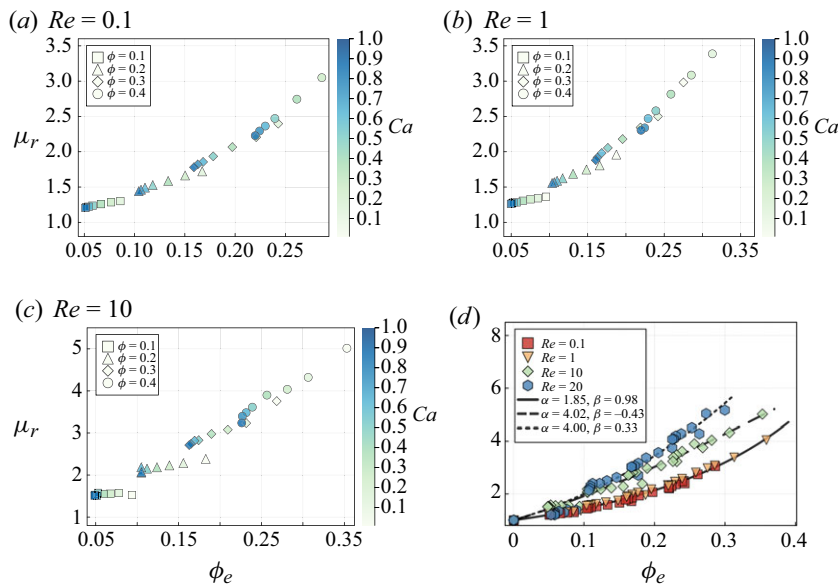
Figure 15. (*a*–*c*) Relative viscosity μ_r of the capsule suspension as a function of ϕ_e. The panels illustrate cases with increasing flow inertia $\mathcal{Re}$; results at different ϕ are represented using distinct markers. (*d*) Prediction of μ_r using Eilers-type model.

$\mathcal{Re}$	α	β	$\langle\epsilon\rangle$	r^2
0.1	1.8518	0.9835	2.3 %	0.9928
1				
10	4.0152	−0.4291	4.1 %	0.9851
20	3.9968	0.3317	7.8 %	0.9764

Table 2. Correlation coefficients α, β, relative error $\langle\epsilon\rangle$ and determination coefficient for Eilers-type models in (5.2).

that in the non-inertial regime. To accurately model the relative viscosity of the capsule suspension, it is essential to consider the effects of inertia and the transition between these two regimes.

Given that the values of μ_r as a function of ϕ_e fall close to a master curve, we can establish new correlations for μ_r using the Eilers-type models in (5.2). For each $\mathcal{Re}$ investigated, we determine the coefficients α and β using the least-square method, as listed in table 2. The prediction results are presented and compared with our computed results in figure 15(*d*). The first observation is that all the numerical data for $\mathcal{Re} = 0.1$ and $\mathcal{Re} = 1$ collapse onto the same master curve (solid black line in figure 15*d*). Consequently, we use the same coefficient set (α, β) for modelling μ_r for these cases in the non-inertial regime, as shown in table 2. The obtained correlation exhibits high accuracy, with an average relative error $\langle\epsilon\rangle = 2.3\,\%$ for $\mathcal{Re} = 0.1$ and $\mathcal{Re} = 1$. In the inertial regime, the effects of $\mathcal{Re}$ on the viscosity evolution become more pronounced, necessitating separate modelling for each $\mathcal{Re}$. The best fit yields a relative error of $\langle\epsilon\rangle = 4.1\,\%$ for $\mathcal{Re} = 10$ and $\langle\epsilon\rangle = 7.8\,\%$ for $\mathcal{Re} = 20$, using the parameters listed in table 2.

Even though Eilers-type models show a promising ability to fit relative viscosity data for suspensions in the non-inertial regime, the dependence on $\mathcal{Re}$ of the model coefficients
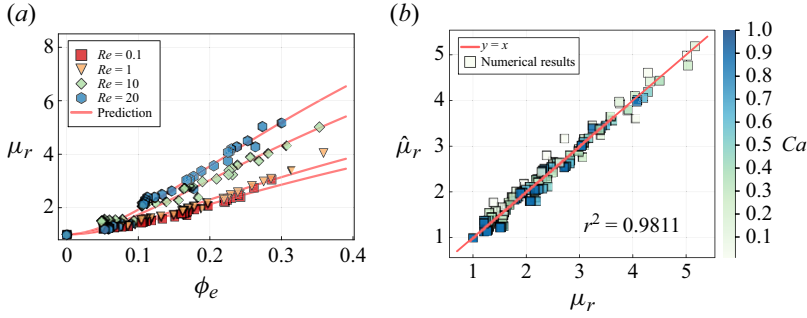
Figure 16. Prediction of models based on the effective volume fraction ϕ_e using the inertia-tuned model.

also makes it less convenient to use and extrapolate at $\mathcal{Re} \geqslant 10$. To address this, we extend the Eilers-type model by introducing an inertia factor of the form $A + B\mathcal{Re}^C$, resulting in the inertia-tuned model

$$\mu_r = 1 + \left(\frac{2.8\phi_e}{1 + 2.59\phi_e} \right)^2 \left(7.92 + 1.65\mathcal{Re}^{0.63} \right). \tag{5.5}$$

Now, with the inertia-tuned model in (5.5), the entire data set is well captured with a single set of coefficients, as shown in figure 16(*a*). The inclusion of the inertia factor allows for accurate prediction of the dependence of μ_r on $\mathcal{Re}$. As shown in figure 16(*b*), the inertia-tuned model in (5.5) achieves a satisfactory determination coefficient of $r^2 = 0.9811$.

Overall, the inertia-tuned model is more physically interpretable and has fewer empirical coefficients than the multivariate correlation in (5.1). However, it is important to note that (5.5) requires the *a priori* computation of the effective volume fraction ϕ_e defined in (5.4). In contrast, the multivariate correlation in (5.1) depends directly on the physical properties of the system: $\mathcal{Re}$, $\mathcal{Ca}$ and ϕ, and does not require the computation of ϕ_e. In general, the correlations and models derived in this section can be of specific interest in different applications, depending on the particular requirements.

5.2.2. *Normal stress of the suspension*

In addition to relative viscosity, we present the evolution of first and second normal stress differences of capsule suspension at $\lambda = 1$ in figure 17. We begin by analysing the particle stress contributions arising from capsule interactions, N_1^p and N_2^p. Subsequently, we take a closer examination of the stress resulting from flow fluctuations, N_1^f and N_2^f.

For the dense suspension at $\phi = 0.4$, the first normal stress difference, N_1^p, predominantly shows positive values except in cases where $\mathcal{Re} \geqslant 10$ and $\mathcal{Ca} = 0.01$, as depicted in figure 17(*a*). Both $\mathcal{Re}$ and $\mathcal{Ca}$ contribute to the increase of N_1^p, with the effect of $\mathcal{Ca}$ being more pronounced in the inertial regime. This trend closely resembles the behaviour of a single capsule in shear flow plotted in figure 8(*d*). The high similarity suggests that the evolution of N_1^p with $\mathcal{Ca}$ in the suspension results from the collective effects of flow inertia on individual capsules. Figures 17(*b*) and 17(*c*) illustrate that a higher ϕ significantly increases N_1^p in both the non-inertial and inertial regimes. Compared with figure 10(*d*–*f*), the observed sign change of N_1^p aligns closely with the variation in the capsule inclination angle $\langle\theta\rangle$, similar to the single capsule case discussed before. The reduction in $\langle\theta\rangle$ from $\pi/4$ (extension axis of shear flow) drives the transition of N_1^p from negative to positive values, particularly pronounced at $\mathcal{Re} = 10$. This phenomenon mirrors
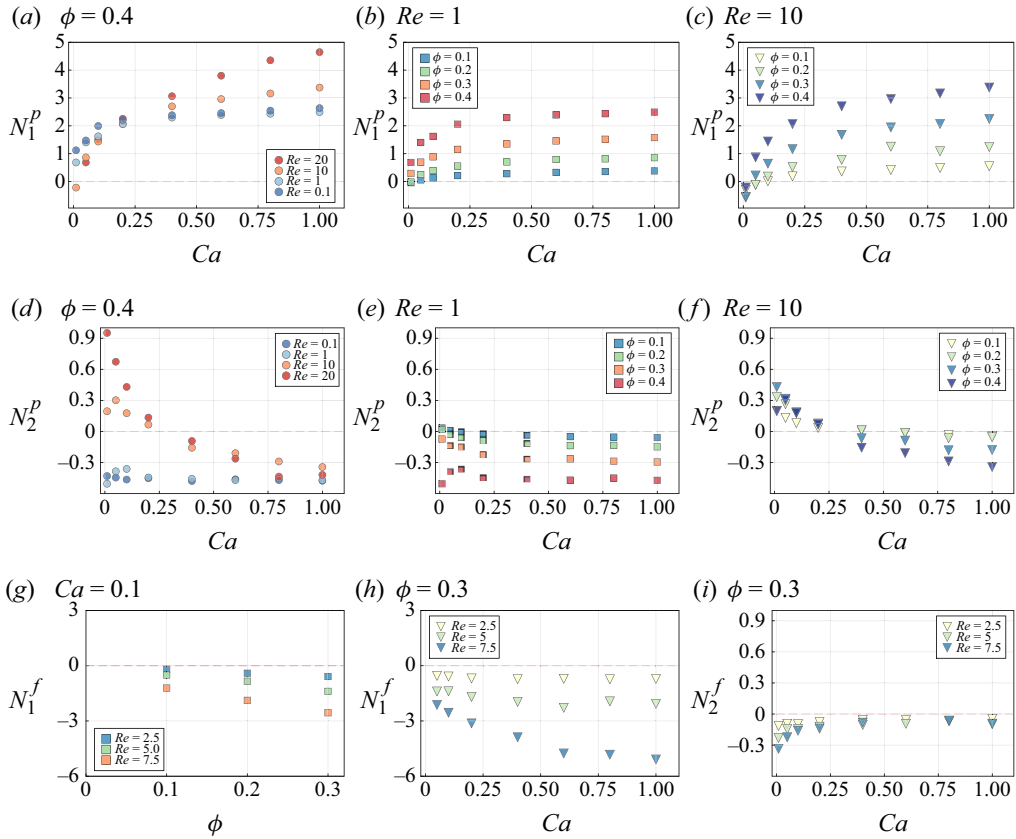
Figure 17. Effects of inertia on the particle stress of capsule suspensions at $\lambda = 1$, $\mathcal{R}e = 0.1 \sim 20$ and $\phi = 0.1 \sim 0.4$. Panels (*a–c*) depict the first normal stress difference N_1^p, panels (*d–f*) illustrate the second normal stress difference N_2^p and panels (*g–i*) present the bulk stress due to flow fluctuation N_1^f and N_2^f.

a similar mechanism identified in both dilute and dense droplet emulsions, as reported by Li & Sarkar (2005*a*) and Srivastava *et al.* (2016). Another possible contribution is the inhomogeneous microstructure of the suspension. Bridge structures often indicate regions of strong interaction and deformation of capsules, which can contribute to the considerable enhancement of particle stress, Σ_{xx}^p, along the streamwise direction in inertial flow, thus increasing N_1^p.

Regarding N_2^p, we observe a decreasing trend as a function of Ca at $\phi = 0.4$ in figure 17(*d*). At $\mathcal{R}e \leqslant 1$, N_2^p exhibits negative values at high ϕ, different from the positive values observed in the single capsule case in figure 8(*g*). The enhanced flow inertia at $\mathcal{R}e \geqslant 10$ results in positive N_2^p at small Ca. In figure 17(*e*), we note that a high volume fraction ϕ leads to a significant decrease in N_2^p at $\mathcal{R}e = 1$. The negative values of N_2^p indicate that the increase in normal stress along the z-axis is more significant than along the y-axis as ϕ increases. From the point of view of the suspension microstructure, the capsules forming the bridge structures provide ample free space for other capsules in the shear plane, potentially reducing the overall normal stress Σ_{yy}^p in the gradient direction. In contrast, along the z-axis, the normal stress Σ_{zz}^p increases with ϕ due to the rise in binary interactions. At $\mathcal{R}e = 10$ in figure 17(*f*), the sign change of N_2^p occurs at $0.2 \leqslant Ca \leqslant 0.4$, distinct from that of N_1^p, as it does not directly correlate with the inclination angle $\langle \theta \rangle$.

The evolution of bulk stress due to flow fluctuations is presented in figures 17(*g*)–17(*i*). The shear stress Σ_{xy}^{f} is significantly smaller compared with Σ_{xy}^{p} and is therefore not plotted here. Flow fluctuations predominantly impact the first normal stress difference, N_1^{f}, whose magnitude increases with ϕ, as shown in figure 17(*g*). Unlike N_1^{p}, N_1^{f} exhibits negative values for ϕ in the range of 0.1 to 0.3. Intuitively, increasing $\mathcal{R}e$ amplifies the magnitude of N_1^{f}. At $\phi = 0.3$, figure 17(*h*) illustrates the evolution of N_1^{f} as a function of $\mathcal{C}a$. Higher capsule deformability results in a sharp rise in the magnitude of N_1^{f}, which can surpass N_1^{p}, as shown in figures 17(*b*) and 17(*c*). Conversely, increasing $\mathcal{C}a$ reduces the magnitude of the second normal stress difference, N_2^{f}, as shown in figure 17(*i*). This behaviour arises from the reorientation of capsules along the *x*-axis in more deformable cases, which mitigates stress along the *y* axis.

6. Conclusions

We conducted a comprehensive investigation into the deformation, dynamics and rheology of a single and suspensions of immersed elastic capsules in an inertial shear flow. We performed high-fidelity interface-resolved simulations using octree and multigrid methods to accurately capture the behaviour of elastic capsule suspensions and create an extensive dataset for numerical analysis and modelling.

For a single capsule in the shear flow, we elucidate the promoting effects of flow inertia on capsule deformation and the internal resistance to deformation brought by the viscosity ratio, highlighting the interplay of these two competing factors. We reveal the mechanism behind the stretching of the capsule surface during tank-treading motion. Specifically, we demonstrate that certain critical surface points exhibit constant principal stretches, while others undergo periodic changes. Our study shows that the first and second normal stress differences exhibit a change of sign with increasing flow inertia, indicating a complex interaction between the capsules and the surrounding fluid.

In examining capsule suspensions, the effects of increasing volume fraction on the capsule average deformation, diffusion and rheology are thoroughly discussed. We find the formation of bridge structures due to the pure hydrodynamic interactions among elastic capsules in the shear plane. These interactions enhance the inhomogeneity of the microstructure within the capsule suspension, altering the capsule surface stress distribution and providing new insights into the formation of rouleaux structures in inertial flows. In terms of capsule lateral migration, we identify a critical range of $\mathcal{R}e$ marking the transition of capsule diffusion from the non-inertial regime to the inertial regime, providing a deeper understanding of the underlying mechanisms at play. Furthermore, we reveal close connections between the behaviour of individual capsules and dense suspensions and demonstrate that inertia significantly affects the deformation and rheology of capsule suspensions. We propose multiple new empirical correlations to predict the capsule deformation factor of a single capsule and the relative viscosity of the capsule suspension, which can serve as valuable tools for future research and practical applications.

Our findings enhance the understanding of elastic capsule behaviour in inertial shear flows, paving the way for advances in inertial microfluidic applications. The proposed empirical correlations offer predictive tools to guide the selection of flow parameters, channel geometries and capsule properties, helping to avoid costly and time-intensive trial-and-error processes. These insights enable the customisation of microchannel geometries to meet specific needs, such as isolating tumour cells or bacteria from whole blood, and optimising device designs to reduce clogging. By understanding capsule deformation and

orientation under various shear stresses, device parameters can be precisely tuned to improve separation efficiency and sorting accuracy. The novel insights obtained in this study lay a foundation for future advancements, fostering the development of next-generation inertial microfluidic systems for specific, high-precision applications in healthcare and biotechnology. Future research could extend this work to explore polydisperse capsule suspensions and the behaviour of capsules in channels with complex geometries.

Appendix A. Immersed boundary method

In this study, the membrane is discretised using an unstructured triangulation. Equation (2.5) is resolved via a linear finite element method. Communication between the membrane triangulation and the grid utilises the IBM (Peskin 1977, 2002), where the regularisation of the Dirac distribution in (2.3) employs a smoothed 2-point formulation (Yang *et al.* 2009)

$$
\tilde{\delta}_h(\boldsymbol{x} - \boldsymbol{x_0}) =
\begin{cases}
\dfrac{1}{\tilde{\Delta}^3} \displaystyle\prod_{i=1}^{3} \left(\dfrac{3}{4} - |x_i - x_{0,i}|^2 \right) & \text{if} \quad |x_i - x_{0,i}| \leqslant 0.5 \\[2ex]
\dfrac{1}{\tilde{\Delta}^3} \displaystyle\prod_{i=1}^{3} \left(\dfrac{8}{9} - \dfrac{3}{2}|x_i - x_{0,i}| + \dfrac{1}{2}|x_i - x_{0,i}|^2 \right) & \text{if} \quad 0.5 < |x_i - x_{0,i}| \leqslant 1.5 \\[2ex]
0 & \text{otherwise}
\end{cases}
, \tag{A1}
$$

where $\boldsymbol{x_0} = [x_{0,1}, x_{0,2}, x_{0,3}]$ represents the location of a Lagrangian node on the membrane surface, $x = \tilde{x}/\tilde{\Delta}$ and $\tilde{\Delta}$ is the local mesh size of the Eulerian grid. The prefactor $1/\tilde{\Delta}^3$ ensures that the discrete integral over the entire space, $\int_\Omega \tilde{\delta}_h(\boldsymbol{x_0} - \boldsymbol{x}) \, \mathrm{d}\boldsymbol{x}$, remains equal to one.

The velocity $\tilde{\boldsymbol{V_0}}$ of a Lagrangian node located at $\tilde{\boldsymbol{x_0}}$ is interpolated from the Eulerian velocity field $\tilde{\boldsymbol{u}}$ using

$$
\tilde{\boldsymbol{V_0}} = \sum_{i \in supp(\tilde{\delta}_h(\boldsymbol{x_0} - \boldsymbol{x_i}))} \tilde{\boldsymbol{u_i}} \tilde{\delta}_h(\boldsymbol{x_0} - \boldsymbol{x_i}) \tilde{\Delta}^3, \tag{A2}
$$

where $supp(\tilde{\delta}_h)$ denotes the support of the regularised Dirac delta function. Similarly, the membrane force $\tilde{\boldsymbol{F_0}}$ at a Lagrangian node $\tilde{\boldsymbol{x_0}}$ is distributed to the Eulerian force density function $\tilde{\boldsymbol{f}}$ using (2.3). Once the Lagrangian velocities of all the capsule nodes are interpolated from the Eulerian velocity field using (A2), the position of each node is updated using an explicit forward Euler scheme (Krüger 2012; Aouane *et al.* 2021).

Additionally, when the fluid viscosity inside and outside the capsule membrane differ, we adopt the approach developed by Tryggvason and co-workers (Unverdi & Tryggvason

1992; Tryggvason *et al.* 2001). A discrete indicator $\tilde{\chi}$ is computed from a discrete grid-gradient field $\tilde{\boldsymbol{G}}$

$$\tilde{\boldsymbol{G}}(\boldsymbol{x}) = \sum_{i \in \mathcal{T}} \tilde{\mathcal{A}}_i \tilde{\delta}_h(\boldsymbol{x_0} - \boldsymbol{x_i}) \boldsymbol{n_i}, \tag{A3}$$

where $\mathcal{T}$ denotes the triangular elements on the capsule surface, $\tilde{\mathcal{A}}_i$ is the surface area of triangle i, $\boldsymbol{x_i}$ represents the coordinates of its centroid and $\boldsymbol{n_i}$ is its inward normal vector. By definition, $\tilde{\boldsymbol{G}}$ is non-zero only on the supports of $\tilde{\delta}_h(\boldsymbol{x_0} - \boldsymbol{x_i})$. The discrete indicator function $\tilde{\chi}$ can be computed by solving a Poisson problem

$$\nabla^2 \tilde{\chi} = \nabla \cdot \tilde{\boldsymbol{G}}. \tag{A4}$$

Since $\tilde{\chi}$ is a regularised step function, it remains constant away from the membranes.

Our current implementation of the FTM requires all cells belonging to the supports of $\tilde{\delta}_h(\boldsymbol{x_0} - \boldsymbol{x_i})$ to be the same size $\tilde{\Delta}$. In other words, all Eulerian cells surrounding a membrane must be of uniform size corresponding to the smallest grid size $\tilde{\Delta}$, through adaptive mesh refinement. Note that the volume of the capsule is forced to be conserved in all cases investigated.

Appendix B. Numerical validation of the solver

B.1. *Validation of a single capsule in shear flow*

Figure 18 illustrates the validation of our solver in comparison with the literature for the simulation of a single spherical elastic capsule subjected to a shear flow at $\mathcal{R}e = 0.01$. The viscosity ratio of the capsule studied is unity. We investigate the evolution of the Taylor deformation factor, D, as defined in (2.7) and illustrated in figure 18(*a*). Our simulations align closely with the data reported by (Lac *et al.* 2004; Aouane *et al.* 2021; Guglietta *et al.* 2023). To enhance understanding, we also compute the Taylor deformation factor using an alternate, yet popular, definition

$$D_m = \frac{r_{max} - r_{min}}{r_{max} + r_{min}}, \tag{B1}$$

where r_{max} and r_{min} represent the maximum and minimum radial distances from the capsule's membrane to its centroid within the shear plane. Remarkably, as shown in figure 18(*a*), applying these two definitions at $\mathcal{R}e = 0.01$ results in overlapping curves, demonstrating their consistency. Similar observations extend to the inclination angle of the capsule within the shear plane, as demonstrated in figure 18(*b*). Despite minor discrepancies in θ_m determined by the directions of $\boldsymbol{r}_{max}$ and $\boldsymbol{r}_{min}$ in comparison with the definition by (2.8), the fundamental physical principles continue to hold. In the remainder of the current study, we apply definitions of D and θ using (2.7) and (2.8). In figure 18(*c–e*), we plot the evolution of the lengths of three semi-axis (r_1, r_2, r_3) of the inertia-equivalent ellipsoid in a function of $\mathcal{C}a$. Our numerical results show excellent agreement with existing data reported in the literature (Li & Sarkar 2008; Aouane *et al.* 2021; Guglietta *et al.* 2023).

In terms of validation of forces acting on the capsule membrane, we analyse the particle shear stress Σ_{xy}^p, and the first/second normal stress differences (N_1^p, N_2^p), illustrated in figure 18(*f–h*). Our results indicate that the particle shear stress aligns closely with existing studies (Bagchi & Kalluri 2010; Aouane *et al.* 2021) as shown in figure 18(*f*). A mesh convergence analysis on the first and second normal stress differences N_1^p and N_2^p as functions of $\mathcal{C}a$ is presented in figure 18(*g–h*). We denote n_E and n_L as

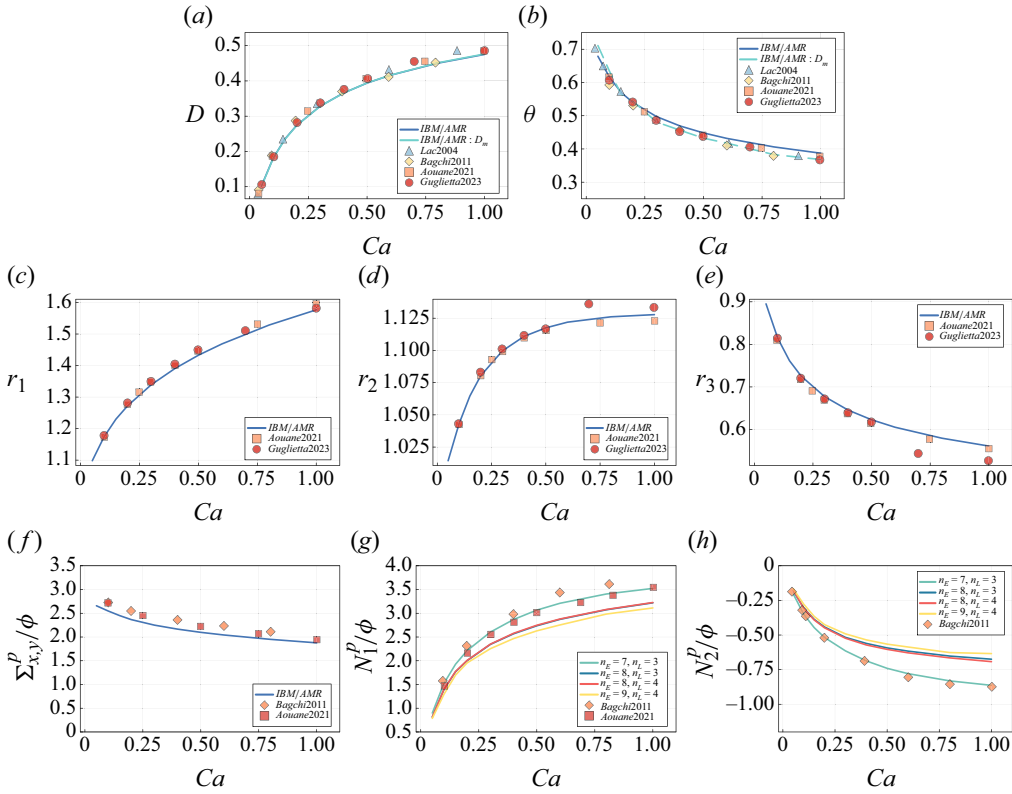Figure 18. Validation of the deformation and particle stress of a single capsule in a shear flow at $\dot{\gamma} = 1$, $\lambda = 1$ and $\mathcal{R}e = 0.01$ as a function of $\mathcal{C}a$; (*a*) Taylor deformation factor, (*b*) inclination angle, (*c-e*) three semi-axis lengths of the moment of inertia equivalent ellipsoid r_1, r_2, r_3, (*f*) particle shear stress Σ_{xy}^p/ϕ and (*g-h*) particle first/second normal stress difference N_1^p/ϕ, N_2^p/ϕ.

the refinement levels of the Eulerian (fluid phase) and Lagrangian (capsule membrane) meshes, respectively. We note that simulations with a coarse mesh ($n_E = 7$, $n_L = 3$) reveal good agreement with the literature. Yet, increasing the mesh resolution modifies the outcomes; for instance, at $n_E = 8$, we observe discrepancies for N_1^p and N_2^p in comparison with the reported findings by (Bagchi & Kalluri 2010; Aouane *et al.* 2021), underscoring their sensitivity to the mesh size. Further elevation of the Eulerian mesh resolution to $n_E = 9$ demonstrates incremental variance in N_1^p and N_2^p. Given this, we opt for $n_E = 8$ and $n_L = 4$ for subsequent simulations of a single capsule in shear flow, a compromise ensuring both high precision and computational efficiency.

B.2. *Validation of capsule suspensions in a shear flow*

Now that the solver is validated for single capsule scenarios, we proceed with simulations to examine the interactions between capsules in a suspension. Figure 19 illustrates the validation of our FTM for a suspension in a shear flow at $\phi = 0.1$ and $\mathcal{R}e = 0.01$ in comparison with data reported in the literature (Aouane *et al.* 2021; Guglietta *et al.* 2023). Our numerical results show a very good agreement with the data reported in Aouane *et al.* (2021) for the three semi-axis lengths of the moment of inertia equivalent ellipsoid, $\langle r_1 \rangle$, $\langle r_2 \rangle$ and $\langle r_3 \rangle$, as seen in figure 19(*a–c*). The symbol $\langle \cdot \rangle$ represents the ensemble average of physical quantities after the flow regime has fully developed. The relative viscosity
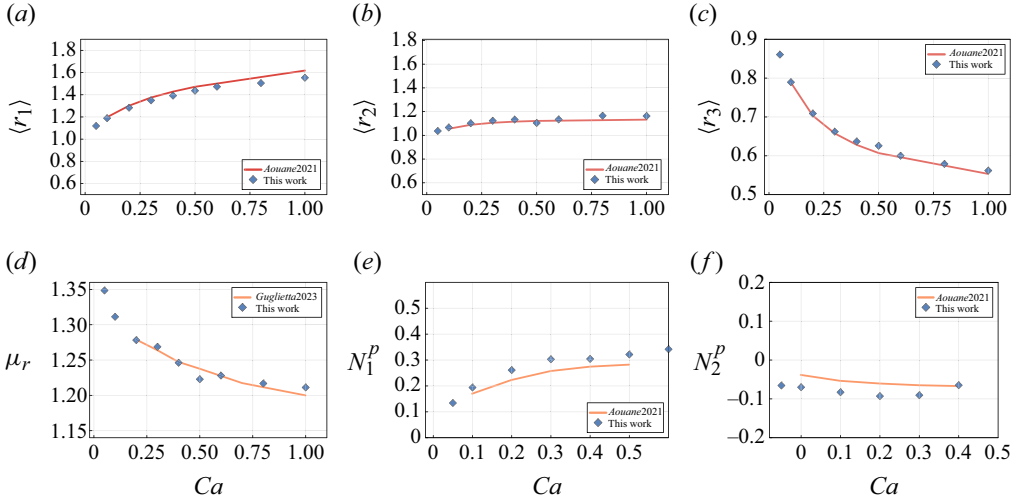
Figure 19. Validation of the deformation and rheology of capsule suspensions in a shear flow at $\dot{\gamma} = 1$, $\lambda = 1$, $\mathcal{R}e = 0.01$ and $\phi = 0.1$ as a function of $\mathcal{C}a$; (*a-c*) three semi-axis lengths of the moment of inertia equivalent ellipsoid $\langle r_1 \rangle$, $\langle r_2 \rangle$, $\langle r_3 \rangle$; (*d*) relative viscosity of the suspension μ_r; (*e-f*) particle first/second normal stress difference N_1^p and N_2^p.

$\langle \mu_r \rangle$, an important aspect of the suspension rheology, is also well captured, as shown in figure 19(*d*). Similar to the single capsule case shown in figure 18(*g–h*), our simulation results for N_1^p and N_2^p show slight differences with those reported in the literature. However, given the higher spatial resolution of our simulations, we are confident that our results are accurate and thoroughly validated.

Appendix C. Repulsive model and its impacts

To prevent capsules from overlapping in a relatively dense suspension, we introduce a repulsive force to simulate the normal component of the lubrication force. This force is activated when the Lagrangian nodes of two neighbouring capsules come into close proximity, specifically when the numerical stencils of the Lagrangian points begin to overlap

$$\tilde{\boldsymbol{f}}_{r,ij} = \begin{cases} \mathcal{K} \left[\left(\frac{2\tilde{\Delta}}{\tilde{d}_{ij}} \right)^2 - 1 \right] \hat{\boldsymbol{d}}_{ij} & \text{if } \tilde{d}_{ij} < 2\tilde{\Delta}, \\ 0 & \text{if } \tilde{d}_{ij} \geqslant 2\tilde{\Delta}. \end{cases} \tag{C1}$$

The repulsive force acts on nodes i and j, which belong to two neighbouring capsules. Let $\tilde{d}_{ij}$ be the distance between these two nodes and $\hat{\boldsymbol{d}}_{ij}$ be the unit vector connecting them. The repulsive coefficient $\mathcal{K} = ||\tilde{\boldsymbol{u}}||/8$ is chosen to be proportional to the local fluid velocity. By implementing this repulsive interaction, we ensure that the capsules maintain a minimum separation distance, preventing any undesired physical overlap.

In figure 20, we show that the macroscopic behaviour of the suspension remains unaffected by the additional repulsive nodal force. We present the temporal evolution of the Taylor deformation factor $\langle D \rangle$ and the relative viscosity μ_r in a dilute suspension of capsules at $\phi = 0.1$ and $\mathcal{R}e = 0.01$. As illustrated in figure 20(*a–b*), the repulsive force model has no impact on the temporal evolution of both $\langle D \rangle$ and μ_r. In this dilute system, the likelihood of interactions between the capsules is low. The ample free space allows the lubrication effects to be well resolved when two capsules encounter each other, effectively
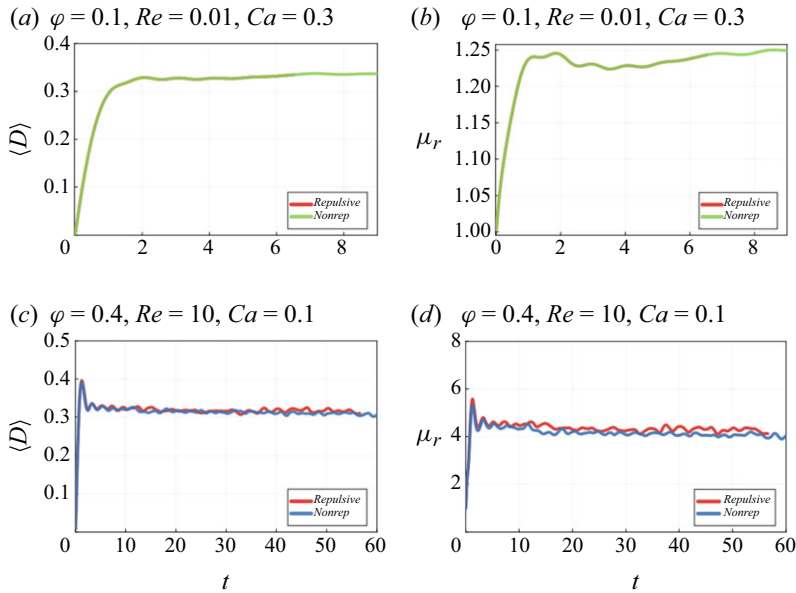
Figure 20. Effects of the repulsive force on the deformation and relative viscosity of the capsule suspension. Panels (*a*) and (*b*) illustrate the effects of the repulsive force on a dilute suspension at $\phi = 0.1$ in the non-inertial regime $\mathcal{R}e = 0.01$, while panels (*c*) and (*d*) show the results for a dense suspension with volume fraction $\phi = 0.4$ in the inertial regime at $\mathcal{R}e = 10$.

preventing them from approaching too closely. As a result, the repulsive model is rarely activated.

In a dense suspension with $\phi = 0.4$ in an inertial flow at $\mathcal{R}e = 10$, interactions among the capsules become significant. As shown in figure 20(*c*), the repulsive force has minor effects on the temporal evolution of the Taylor deformation factor $\langle D \rangle$, while maintaining the same time-averaged value. Similarly, figure 20(*d*) demonstrates that the repulsive force has minor effects only on the temporal evolution of the relative viscosity μ_r, with a relative error of less than 6 % compared with the case without the repulsive force.

To conclude, the repulsive force effectively prevents membrane overlapping and accounts for lubrication effects, thereby enhancing numerical stability. Importantly, this is achieved without altering the dynamics or rheology of the capsule suspension in both the non-inertial and inertial regimes.

Appendix D. Capsule elastic stress in the bridge structure

We plot the capsule elastic stress distribution on the contours of capsules on a cut plane in a suspension with $\phi = 0.3$ in figure 21. The cut plane, perpendicular to the z-axis, is located at $z = 0$ as shown in figure 21(*a*). The capsule contours in this shear plane are coloured based on $\sigma_{2,max}$, with red indicating high stresses and blue indicating low values. From figure 21(*b*), we observe the formation of bridge structures in the suspension. The capsule membrane in the lubrication layer exhibits low $\sigma_{2,max}$ values. The maximum elastic stress, $\sigma_{2,max}$, is observed at the two extremities of the capsule in the shear plane. The bridge structures are temporary because there is no adhesive force holding the capsules together. Without adhesion, the structures are easily broken apart by the shear flow. Despite their temporary nature, the conditions in the shear flow repeatedly bring capsules into close
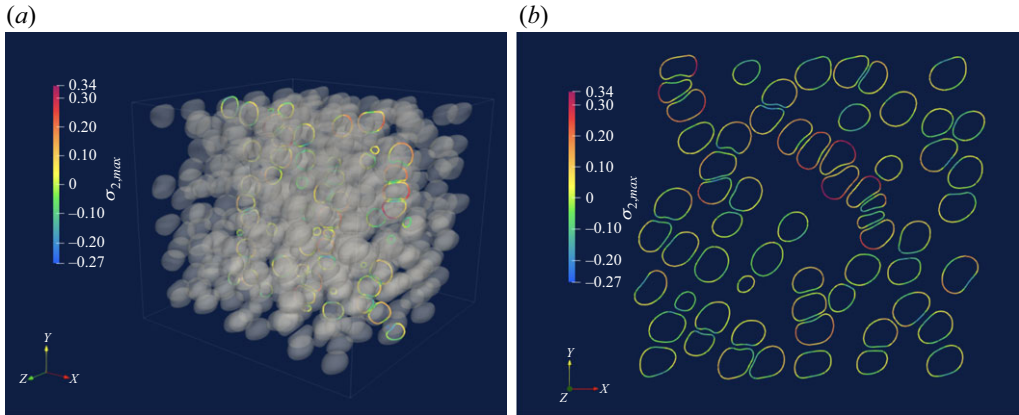
Figure 21. Distribution of the maximum elastic stress $\sigma_{2,max}$ in a capsule suspension at $\phi = 0.3$, $Ca = 0.05$ and $\mathcal{R}e = 0.1$. (*a*) Location of the cut plane in the cubic computation domain, (*b*) snapshot of capsule contours coloured by $\sigma_{2,max}$.

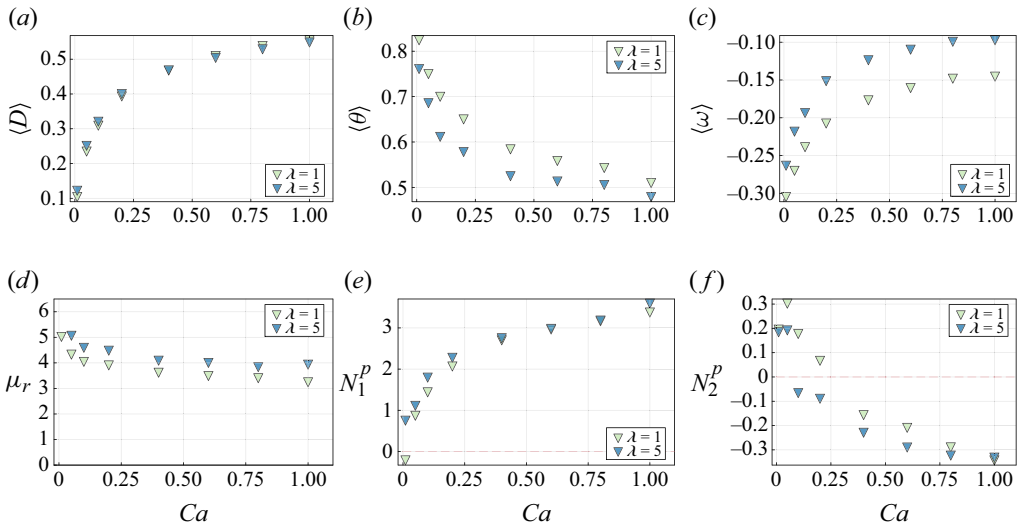Figure 22. Effects of viscosity ratio on the capsule suspensions in a shear flow at $\mathcal{R}e = 10$ and $\phi = 0.4$. (*a*) Ensemble-averaged Taylor deformation factor $\langle D \rangle$, (*b*) inclination angle $\langle \theta \rangle$, (*c*) tank-treading velocity $\langle \omega \rangle$, (*d*) relative viscosity μ_r, (*e*) first normal stress difference N_1^p and (*e*) second normal stress difference Σ_{xy}^p.

proximity, leading to the frequent formation of bridge structures, due to the hydrodynamic forces in the suspension.

Appendix E. Effects of viscosity ratio on capsule suspension

We briefly present and discuss the effects of the viscosity ratio λ on capsule suspensions at $\phi = 0.4$ and $\mathcal{R}e = 10$ in figure 22. Generally, the effects of λ on a dense suspension are minor compared with the effects of ϕ discussed in §5. As shown in figure 22(*a*), increasing the viscosity ratio from $\lambda = 1$ to $\lambda = 5$ barely changes the average deformation $\langle D \rangle$ of the suspension. However, the inclination angle $\langle \theta \rangle$ and the magnitude of the tank-treading velocity $\langle \omega \rangle$ are reduced due to the increased resistance in the internal fluid of the capsules. Regarding particle stresses, we observe a slight increase in the relative viscosity μ_r in figure 22(*d*), which is opposite to the effect of λ in the single capsule case, as depicted
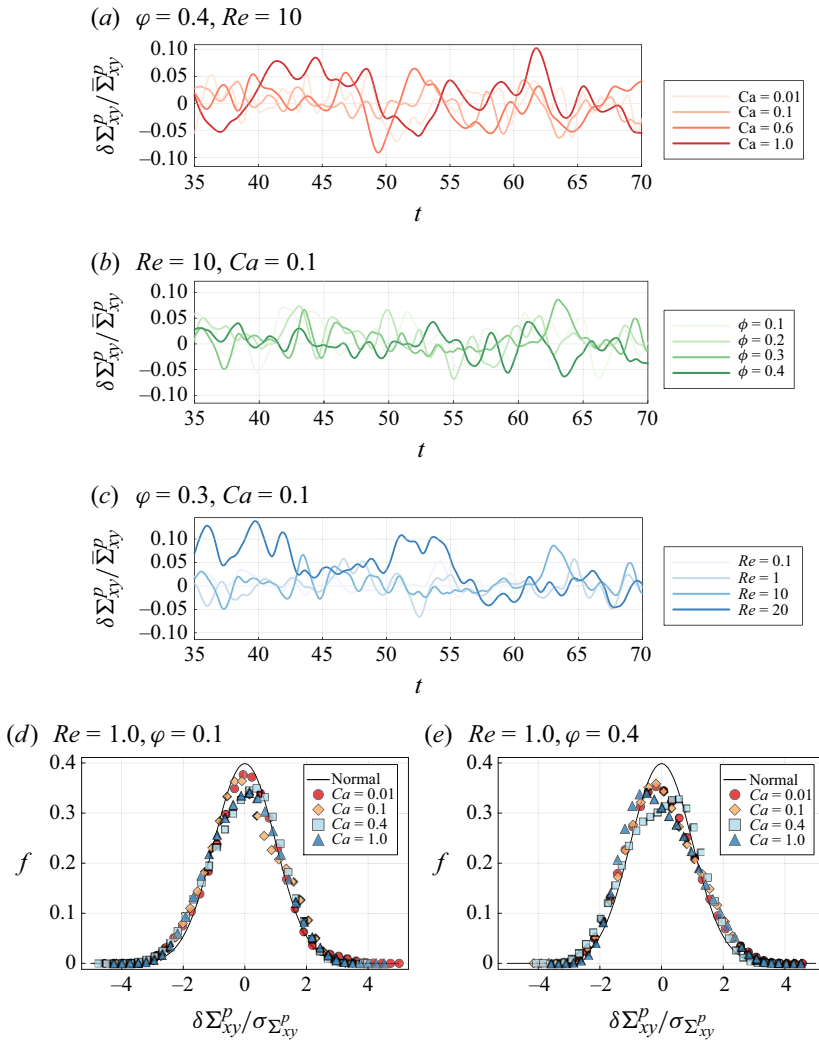
Figure 23. Shear stress fluctuation of the capsule suspension. (*a-c*) Temporal evolution of the shear stress under effects of $\mathcal{Ca}$, ϕ and $\mathcal{Re}$, respectively; (*d-e*) probability distribution function f of particle shear stress fluctuations at $\phi = 0.1$ and $\phi = 0.4$; a reference normal distribution is presented in black solid line. Here, $\sigma_{\Sigma^p_{xy}}$ denotes the standard deviation of the particle shear stress Σ^p_{xy}.

in figure 8(*c*). This increase can be attributed to the enhanced short-range interactions among the suspended capsules due to the higher internal viscosity at a higher λ. In terms of the normal stress differences, λ shows only a minor impact on the evolution of N^p_1 in figure 22(*e*), although a slight decrease in N^p_2 is observed at a higher viscosity ratio $\lambda = 5$ in figure 22(*f*). In the non-inertial regime, we observe similar effects of λ, so the numerical results are not presented for brevity.

Appendix F. Fluctuations of the shear stress

Due to the inhomogeneous microscopic structure of the capsule suspension, the particle shear stress consistently fluctuates around the average value, once the flow is fully

developed

$$\Sigma_{xy}^p = \overline{\Sigma}_{xy}^p + \delta\Sigma_{xy}^p, \tag{F1}$$

where $\overline{\Sigma}_{xy}^p$ and $\delta\Sigma_{xy}^p$ denote the time-averaged shear stress and its fluctuations, respectively. Figure 23(*a*–*c*) presents the temporal evolution of the shear stress fluctuations at different $\mathcal{C}a$, ϕ and $\mathcal{R}e$. We observe that higher deformability of the capsules leads to increased shear stress fluctuations $\delta\Sigma_{xy}^p$ at $\mathcal{R}e = 10$ and $\phi = 0.4$ in figure 23(*a*). In the inertial regime, ϕ has minor effects on $\delta\Sigma_{xy}^p$ as shown in figure 23(*b*). However, an increase in $\mathcal{R}e$ results in a significant rise in shear stress fluctuations in figure 23(*c*). Generally, $\delta\Sigma_{xy}^p$ represents less than 15 % of the total shear stress Σ_{xy}^p even at $\mathcal{R}e = 20$.

Regarding the distribution of stress fluctuations, figure 23(*d*) shows that at low Reynolds number ($\mathcal{R}e = 1$), low volume fraction ($\phi = 0.1$) and low capillary number ($\mathcal{C}a = 0.01$), $\delta\Sigma_{xy}^p$ follows a normal distribution with an average value of zero. Increasing $\mathcal{C}a$ causes deviations from this normal distribution, leading to a lower peak value as seen in figure 23(*d*). In a dense suspension ($\phi = 0.4$), there is a clear deviation from the normal distribution for all investigated $\mathcal{C}a$ values, as shown in figure 23(*e*). Higher $\mathcal{R}e$ also causes deviations from the normal distribution, although these results are not shown here for brevity.

REFERENCES

AMINI, H., LEE, W. & DI CARLO, D. 2014 Inertial microfluidic physics. *Lab Chip* **14** (15), 2739–2761.
AOUANE, O., SCAGLIARINI, A. & HARTING, J. 2021 Structure and rheology of suspensions of spherical strain-hardening capsules. *J. Fluid Mech.* **911**.A11.
BAGCHI, P. & KALLURI, R.M. 2010 Rheology of a dilute suspension of liquid-filled elastic capsules. *Phys. Rev. E Stat. Nonlinear Soft Matt. Phys.* **81** (5 Pt 2), 056320.
BALOGH, P. & BAGCHI, P. 2017 A computational approach to modeling cellular-scale blood flow in complex geometry. *J. Comput. Phys.* **334**, 280–307.
BALOGH, P. & BAGCHI, P. 2018 Analysis of red blood cell partitioning at bifurcations in simulated microvascular networks. *Phys. Fluids* **30** (5), 051902.
BALOGH, P. & BAGCHI, P. 2019 The cell-free layer in simulated microvascular networks. *J. Fluid Mech.* **864**, 768–806.
BALOGH, P., GOUNLEY, J., ROYCHOWDHURY, S. & RANDLES, A. 2021 A data-driven approach to modeling cancer cell mechanics during microcirculatory transport. *Sci. Rep.* **11** (1), 1–18.
BANAEI, A.A., LOISEAU, J.-C., LASHGARI, I. & BRANDT, L. 2017 Numerical simulations of elastic capsules with nucleus in shear flow. *Eur. J. Comput. Mech.* **26** (1–2), 131–153.
BANAEI, A.A., SHAHMARDI, A. & BRANDT, L. 2021 Numerical study of suspensions of nucleated capsules at finite inertia. *Phys. Rev. Fluids* **6**, 044301.
BARTHES-BIESEL, D. 2016 Motion and deformation of elastic capsules and vesicles in flow. *Annu. Rev. Fluid Mech.* **48**, 25–52.
BARTHES-BIESEL, D. & RALLISON, J.M. 1981 The time-dependent deformation of a capsule freely suspended in a linear shear flow. *J. Fluid Mech.* **113**, 251–267.
BATCHELOR, G.K. 1970 The stress system in a suspension of force-free particles. *J. Fluid Mech.* **41** (3), 545–570.
BATCHELOR, G.K. & GREEN, J.T. 1972 The determination of the bulk stress in a suspension of spherical particles to order c2. *J. Fluid Mech.* **56** (3), 401–427.
BISHOP, J.J., POPEL, A.S., INTAGLIETTA, M. & JOHNSON, P.C. 2002 Effect of aggregation and shear rate on the dispersion of red blood cells flowing in venules. *Am. J. Physiol. Heart Circ. Physiol.* **283** (5), H1985–H1996.
BREEDVELD, V. 2000 Shear-induced self-diffusion in concentrated suspensions. *PhD thesis*, University of Twente.
CHINCHILLA, L., ARMSTRONG, C., MEHRI, R., SAVOIA, A.S., FENECH, M. & FRANCESCHINI, E. 2021 Numerical investigations of anisotropic structures of red blood cell aggregates on ultrasonic backscattering. *J. Acoust. Soc. Am.* **149** (4), 2415.
DODDI, S.K. & BAGCHI, P. 2008 Effect of inertia on the hydrodynamic interaction between two liquid capsules in simple shear flow. *Int. J. Multiph. Flow* **34** (4), 375–392.

EBRAHIMI, S. & BAGCHI, P. 2021 Inertial and non-inertial focusing of a deformable capsule in a curved microchannel. *J. Fluid Mech.* **929**, 1–38.

ECKSTEIN, E.C., BAILEY, D.G. & SHAPIRO, A.H. 1977 Self-diffusion of particles in shear flow of a suspension. *J. Fluid Mech.* **79** (1), 191–208.

EINSTEIN, A. 1911 Berichtigung zu meiner arbeit: eine neue bestimmung der moleküldimensionen. *Annalen der Physik* **339** (3), 591–592.

GEKLE, S. 2016 Strongly accelerated margination of active particles in blood flow. *Biophys. J.* **110** (2), 514–520.

GROSS, M., KRÜGER, T. & VARNIK, F. 2014 Rheology of dense suspensions of elastic capsules: normal stresses, yield stress, jamming and confinement effects. *Soft Matt.* **10** (24), 4360–4372.

GROSS, M., KRÜGER, T. & VARNIK, F. 2015 Fluctuations and diffusion in sheared athermal suspensions of deformable particles. *Epl-EUROPHYS. Lett.* **108** (6), 68006.

GUBSPUN, J., GIRES, P.-Y., DE LOUBENS, C., BARTHES-BIESEL, D., 2016 Characterization of the mechanical properties of cross-linked serum albumin microcapsules: effect of size and protein concentration. *Colloid Polym. Sci.* **294** (8), 1381–1389.

GUGLIETTA, F., PELUSI, F., SEGA, M., AOUANE, O. & HARTING, J. 2023 Suspensions of viscoelastic capsules: effect of membrane viscosity on transient dynamics. *J. Fluid Mech.* **971**, A13.

HADDADI, H. & MORRIS, J.F. 2014 Microstructure and rheology of finite inertia neutrally buoyant suspensions. *J. Fluid Mech.* **749**, 431–459.

HÄNER, E., VESPERINI, D., SALSAC, A.-V., LE GOFF, A. & JUEL, A. 2021 Sorting of capsules according to their stiffness: from principle to application. *Soft Matt.* **17** (13), 3722–3732.

HUET, D.P., MORENTE, A., GAI, G. & WACHS, A. 2024 Motion and deformation of capsules flowing through a corner in the inertial and non-inertial regimes. *Phys. Rev. Fluids* **9**, 053601.

HUET, D.P. & WACHS, A. 2023 A cartesian-octree adaptive front-tracking solver for immersed biological capsules in large complex domains. *J. Comput. Phys.* **492**, 112424.

KILIMNIK, A., MAO, W. & ALEXEEV, A. 2011 Inertial migration of deformable capsules in channel flow. *Phys. Fluids* **23** (12), 123302.

KRÜGER, T. 2012 *Computer Simulation Study of Collective Phenomena in Dense Suspensions of Red Blood Cells under Shear*. Springer Science & Business Media.

KRÜGER, T., KAOUI, B. & HARTING, J. 2014 Interplay of inertia and deformability on rheological properties of a suspension of capsules. *J. Fluid Mech.* **751**, 725–745.

KULKARNI, P.M. & MORRIS, J.F. 2008 Suspension properties at finite reynolds number from simulated shear flow. *Phys. Fluids* **20** (4), 040602.

LAC, E., BARTHES-BIESEL, D., PELEKASIS, N.A. & TSAMOPOULOS, J. 2004 Spherical capsules in three-dimensional unbounded stokes flows: effect of the membrane constitutive law and onset of buckling. *J. Fluid Mech.* **516**, 303–334.

LEE, C.-A. & PAENG, D.-G. 2021 Numerical simulation of spatiotemporal red blood cell aggregation under sinusoidal pulsatile flow. *Sci. Rep.* **11** (1), 9977.

LEIGHTON, D. & ACRIVOS, A. 1987 The shear-induced migration of particles in concentrated suspensions. *J. Fluid Mech.* **181**, 415–439.

LI, X. & SARKAR, K. 2005a Effects of inertia on the rheology of a dilute emulsion of drops in shear. *J. Rheol.* **49** (6), 1377–1394.

LI, X. & SARKAR, K. 2005b Negative normal stress elasticity of emulsions of viscous drops at finite inertia. *Phys. Rev. Lett.* **95** (25), 256001.

LI, X. & SARKAR, K. 2008 Front tracking simulation of deformation and buckling instability of a liquid capsule enclosed by an elastic membrane. *J. Comput. Phys.* **227** (10), 4998–5018.

LUO, Z.Y. & BAI, B.F. 2019 Solute release from an elastic capsule flowing through a microfluidic channel constriction. *Phys. Fluids* **31** (12), 121902.

MWASAME, P.M., WAGNER, N.J. & BERIS, A.N. 2017 On the macroscopic modelling of dilute emulsions under flow. *J. Fluid Mech.* **831**, 433–473.

OLAPADE, P.O., SINGH, R.K. & SARKAR, K. 2009 Pairwise interactions between deformable drops in free shear at finite inertia. *Phys. Fluids* **21** (6), 063302.

OWEN, B. 2023 Lattice-boltzmann modelling for inertial particle microfluidics applications - a tutorial review. *Adv. Phys. X* **8** (1), 2246704.

PESKIN, C.S. 1977 Numerical analysis of blood flow in the heart. *J. Comput. Phys.* **25** (3), 220–252.

PESKIN, C.S. 2002 The immersed boundary method. *Acta Numerica* **11** (1), 479–517.

POPINET, S. 2015 A quadtree-adaptive multigrid solver for the Serre–Green–Naghdi equations. *J. Comput. Phys.* **302**, 336–358.

POZRIKIDIS, C. 1995 Finite deformation of liquid capsules enclosed by elastic membranes in simple shear flow. *J. Fluid Mech.* **297**, 123–152.

POZRIKIDIS, C. 2001 Effect of membrane bending stiffness on the deformation of capsules in simple shear flow. *J. Fluid Mech.* **440**, 269–291.

RAFFIEE, A.H., DABIRI, S. & ARDEKANI, A.M. 2017 Elasto-inertial migration of deformable capsules in a microchannel. *Biomicrofluidics* **11** (6), 064113.

RAHMANI, M., HAMMOUTI, A. & WACHS, A. 2018 Momentum balance and stresses in a suspension of spherical particles in a plane Couette flow. *Phys. Fluids* **30** (4), 043301.

RAJA, R.V., SUBRAMANIAN, G. & KOCH, D.L. 2010 Inertial effects on the rheology of a dilute emulsion. *J. Fluid Mech.* **646**, 255–296.

RAMANUJAN, S. & POZRIKIDIS, C. 1998 Deformation of liquid capsules enclosed by elastic membranes in simple shear flow: large deformations and the effect of fluid viscosities. *J. Fluid Mech.* **361**, 117–143.

ROSTI, M.E., BRANDT, L. & MITRA, D. 2018 Rheology of suspensions of viscoelastic spheres: Deformability as an effective volume fraction. *Phys. Rev. Fluids* **3** (1), 012301.

SINGH, R.K. & SARKAR, K. 2009 Effects of viscosity ratio and three dimensional positioning on hydrodynamic interactions between two viscous drops in a shear flow at finite inertia. *Phys. Fluids* **21** (10), 103303.

SINGH, R.K. & SARKAR, K. 2011 Inertial effects on the dynamics, streamline topology and interfacial stresses due to a drop in shear. *J. Fluid Mech.* **683**, 149–171.

SINGH, R.K. & SARKAR, K. 2015 Hydrodynamic interactions between pairs of capsules and drops in a simple shear: effects of viscosity ratio and heterogeneous collision. *Phys. Rev. E* **92** (6), 063029.

SINGH, R.K., LI, X. & SARKAR, K. 2014 Lateral migration of a capsule in plane shear near a wall. *J. Fluid Mech.* **739**, 421–443.

SON, J., SAMUEL, R., GALE, B.K., CARRELL, D.T. & HOTALING, J.M. 2017 Separation of sperm cells from samples containing high concentrations of white blood cells using a spiral channel. *Biomicrofluidics* **11** (5), 054106.

SRIVASTAVA, P., MALIPEDDI, A.R. & SARKAR, K. 2016 Steady shear rheology of a viscous emulsion in the presence of finite inertia at moderate volume fractions: sign reversal of normal stress differences. *J. Fluid Mech.* **805**, 494–522.

SUN, F.-C., FU, J.-H., PENG, Y.-X., JIAO, X.-M., LIU, H., DU, F.-P. & ZHANG, Y.-F. 2021 Dual-functional intumescent fire-retardant/self-healing water-based plywood coatings. *Prog. Org. Coat.* **154**, 106187.

TAKEISHI, N., ROSTI, M.E., IMAI, Y., WADA, S. & BRANDT, L. 2019 Haemorheology in dilute, semi-dilute and dense suspensions of red blood cells. *J. Fluid Mech.* **872**, 818–848.

TRYGGVASON, G., BUNNER, B., ESMAEELI, A., JURIC, D., AL-RAWAHI, N., TAUBER, W., HAN, J., NAS, S. & JAN, Y.-J. 2001 A front-tracking method for the computations of multiphase flow. *J. Comput. Phys.* **169** (2), 708–759.

UNVERDI, S.O. & TRYGGVASON, G. 1992 A front-tracking method for viscous, incompressible, multi-fluid flows. *J. Comput. Phys.* **100** (1), 25–37.

WANG, Z., SUI, Y., SALSAC, A.-V., BARTHÈS-BIESEL, D. & WANG, W. 2016 Motion of a spherical capsule in branched tube flow with finite inertia. *J. Fluid Mech.* **806**, 603–626.

YANG, X., ZHANG, X., LI, Z. & HE, G.-W. 2009 A smoothing technique for discrete delta functions with application to immersed boundary method in moving boundary simulations. *J. Comput. Phys.* **228** (20), 7821–7836.

YIN, J., WANG, Z., LI, G., LIN, F., SHAO, K., CAO, B. & HOU, Y. 2019 Characterization of circulating tumor cells in breast cancer patients by spiral microfluidics. *Cell Biol. Toxicol.* **35** (1), 59–66.

ZHU, L., RORAI, C., MITRA, D. & BRANDT, L. 2014 A microfluidic device to sort capsules by deformability: a numerical study. *Soft Matt.* **10** (39), 7705–7711.